

Syracuse University

SURFACE at Syracuse University

Theses - ALL

11-3-2016

Mechanistic Investigation Toward A Microkinetic Model For Decarboxylation Of Gamma Valerolactone Over Silica Alumina

Christian Suhngwa Jungong
Syracuse University

Follow this and additional works at: <https://surface.syr.edu/thesis>

 Part of the [Chemical Engineering Commons](#)

Recommended Citation

Jungong, Christian Suhngwa, "Mechanistic Investigation Toward A Microkinetic Model For Decarboxylation Of Gamma Valerolactone Over Silica Alumina" (2016). *Theses - ALL*. 782.
<https://surface.syr.edu/thesis/782>

This Thesis is brought to you for free and open access by SURFACE at Syracuse University. It has been accepted for inclusion in Theses - ALL by an authorized administrator of SURFACE at Syracuse University. For more information, please contact surface@syr.edu.

ABSTRACT

γ -valerolactone (GVL) ring opening- and decarboxylation rates were measured over amorphous silica alumina ($\text{SiO}_2/\text{Al}_2\text{O}_3$) catalyst in the gas phase, using a down configuration fixed bed reactor, operating under anhydrous and differential conditions. By varying temperature, space time and GVL partial pressure, measured rates were leveraged to determine kinetic parameters (apparent activation barriers and pre-exponential factors) for the ring opening and decarboxylation step, as well as thermodynamic parameters (enthalpy- and entropy of reaction) for the ring opening step. The experimentally measured parameters were applied for the development of a microkinetic model that quantitatively describes the overall kinetics involved in the decarboxylation of GVL over $\text{SiO}_2/\text{Al}_2\text{O}_3$. The microkinetic model predicts that the adsorption of GVL onto the surface of the catalyst and the subsequent ring opening step are two main elementary steps driving the kinetics of the process. In addition, the equilibrium constant of the adsorption step and apparent forward rate constant for the ring opening step were predicted as key parameters associated with the decarboxylation event. By comparing model predicted apparent forward rate constants for all relevant elementary steps involved in the mechanism of GVL decarboxylation, the ring opening step was identified as the slowest step; hence it's probably the rate determining step. In previous studies, decarboxylation of GVL over aluminosilicates with comparable apparent activation barriers and deprotonation energies revealed markedly different turn over frequencies; the microkinetic model introduced suggests that the difference in turn over frequencies is an artifact of local structural effects in the vicinity of the acid site. Although the model describes the kinetics involved, testing more aluminosilicates with different pore sizes will provide more information about the relative importance of the surface adsorption and ring opening steps.

MECHANISTIC INVESTIGATION TOWARD A MICROKINETIC MODEL FOR
DECARBOXYLATION OF GAMMA VALEROLACTONE OVER SILICA ALUMINA

by

Christian Suhngwa Jungong

B.S., University of Buea, 2006
PhD, University of North Dakota, 2012

Thesis

Submitted in partial fulfillment of the requirements for the degree of
Master of Science in Chemical Engineering

Syracuse University
May 2016

Copyright © Christian Suhngwa Jungong 2016

All rights reserved

ACKNOWLEDGEMENTS

Doing research is never an isolated effort and though the cover of this thesis bears only my name, it would never have been completed without the help of several individuals who made valuable contributions directly and indirectly. Regrettably, I cannot acknowledge them all by name. Many thanks to all those who have made my experience at Syracuse University one that I would cherish and remember.

I would like to express my deepest gratitude to my advisor, Prof Jesse Bond, for his mentorship, encouragement, and support. I am grateful for the opportunity you gave me to work in your lab, and I have really enjoyed learning about reaction engineering and chemical kinetics. It wasn't easy transitioning from an organic chemistry lab to a chemical engineering lab, but your patience and continual guidance made it effortless and I am particularly grateful.

I like to thank all the other members of my thesis committee-- not just for taking the time to be a part of the oral examination process-- but also for proofreading this thesis and clarifying my thoughts about the project. I will always be thankful to the staff and faculty of the Department of Biomedical and Chemical Engineering who ensured that my collegiate experience in the department was positive and rewarding.

It would have been a lonely lab without my group members. Argy, Omar, Josh, Shaofu, Siddhart, Ran and Xinlei I cannot thank you guys enough for the fun, continual support and warm humor. You made it worthwhile for me coming in to lab everyday.

Finally, I am indebted to my friends and family for the sacrifices, moral support, and encouragement they offered while I worked on this thesis. In particular, I am especially thankful to my parents for the countless and thankless sacrifices they have made over the years to ensure that I succeed in my endeavors. This achievement is truly yours.

TABLE OF CONTENTS

ACKNOWLEDGEMENTS	iv
LIST OF FIGURES	vii
LIST OF TABLES	ix
LIST OF ABBREVIATIONS AND ACRONYMS	x
CHAPTER.....	1
I. INTRODUCTION	1
II. LITERATURE REVIEW	9
2.1. Structure and properties of γ -valerolactone (GVL).....	9
2.2. Production of GVL from lignocellulose biomass.....	10
2.3. Derivatives of γ -valerolactone.....	15
2.4 Decarboxylation of GVL.....	17
2.4.1 Mechanism of GVL decarboxylation.....	17
2.4.2. Kinetics of decarboxylation of GVL.....	20
2.5. Intrinsic behavior of different solid acids during decarboxylation	22
III MATERIALS AND METHODS	27
3.1 Materials.....	27
3.2 Catalyst characterization	27
3.3 Decarboxylation of GVL and PEA over $\text{SiO}_2/\text{Al}_2\text{O}_3$ (DAVICAT SIAL 3113).....	28
3.3 Development of microkinetic model.....	34
IV RESULTS AND DISCUSSION	35
4.1 Catalyst activity vs time on stream.....	35

4.2. Interconversion between GVL and PEA isomers.....	37
4.2.1 Partial pressure dependence	37
4.2.2. Determination of equilibrium conversion	38
4.2.3. Determination of kinetic and thermodynamic parameters	40
4.3 GVL and PEA decarboxylation.....	49
4.4. Development of microkinetic model.....	52
4.4.1. Decarboxylation landscape	53
4.4.2 Estimation of equilibrium constants	58
4.4.3 Estimation of forward rate constants	59
4.4.4 Microkinetic model calibration.....	60
V CONCLUSION AND FUTURE DIRECTION.....	64
5.1 Conclusion.....	64
REFERENCES	66
VITA.....	73

LIST OF FIGURES

Figure	Page
1. Carbon cycles for petroleum- and bio-refinery.	3
2. Structural composition of biomass feedstocks (copied from ref 6b).	4
3. Composition of lignocellulosic biomass (adopted from ref 9).	5
4. Lignocellulosic biomass processing platforms (adopted from ref 11a).	7
5. Molecular structure of GVL.	9
6. Production of GVL from lignocellulosic biomass (copied from ref 37).	11
7. Schematic of high-value derivatives from GVL (copied from ref 49a).	15
8. GVL decarboxylation pathways.	19
9. Schematic representation of experimental apparatus.	29
10. Mass-normalized production rates of PEA isomers as a function of time on stream; 2.8 mbar partial pressure of GVL; T = 443.15 K, space time (τ) = 15.75 min, 1.0 bar, and 1004 mg SiO ₂ /Al ₂ O ₃	36
11. Dependence of ring opening and decarboxylation on partial pressure of GVL; T = 441.15 K, τ = 3.94 min, 1 bar.	38
12. Determination of equilibrium conversion of GVL to PEA isomers on SiO ₂ /Al ₂ O ₃ , at 471 K, 1 bar, 10 mbar of GVL partial pressure.	39
13. Conversion of GVL to butene isomers on SiO ₂ /Al ₂ O ₃ , at 471 K, 1 bar, and 10 mbar of GVL partial pressure.	40
14. Measured outlet PEA to GVL ratio on SiO ₂ /Al ₂ O ₃ , at 471 K, 1 bar, 10 mbar of GVL partial pressure.	41
15. Estimated forward rate constants at different temperatures.	46
16. Estimated equilibrium constants at different temperatures.	46
17. Relationship between activation energy and enthalpy of reaction during GVL to PEA interconversion.	47

18. Conversion of PEA to GVL as a function of space time, 441 K, SiO ₂ /Al ₂ O ₃ , 10 mbar PEA partial pressure	48
19. Apparent reverse rate constants of PEA ring closure to GVL as a function of temperature.	49
20. Decarboxylation rates of PEA and GVL introduced independently over SiO ₂ /Al ₂ O ₃ , at 10 mbar partial pressure, respectively and at different temperatures	51
21. GVL reaction landscape over SiO ₂ /Al ₂ O ₃	53

LIST OF TABLES

Table	Page
1. Physical and chemical properties of GVL ^{25, 29}	10
2. Mole balance for reversible equilibrium between GVL and PEA isomers	42
3. Estimated forward rate constants and equilibrium constants from PFR model.	45
4. Apparent reverse rate constants for PEA ring closure to GVL at various temperatures.	48
5. Theoretical decarboxylation rates at zero time on stream using PEA and GVL independently, as reactant feeds (10 mbar)	50
6. Summary of kinetic and thermodynamic parameters determined experimentally	52
7. Degree of rate control for key elementary steps.....	61
8. Degree of thermodynamic rate control for key intermediates.....	62

LIST OF ABBREVIATIONS AND ACRONYMS

a_j	Activity of species j
AL-MCM-41	Aluminum containing mobile crystalline material
Al_2O_3	Alumina
ASA	Amorphous silica alumina
ASAP	Accelerated surface area and porosimetry system
BET	Brunauer-Emmett-Teller
BJH	Barret-Joyner-Halenda
CH_4	Methane
CO	Carbon monoxide
CO_2	Carbon dioxide
CSTR	Continuously stirred tank reactor
Cu	Copper
DC	Decarboxylation rate
E_A	Apparent activation energy
FID	Flame ionization detector
f_j	Fugacity of species j
GC	Gas chromatograph
GVL	γ -valerolactone
h	Planck's constant
H-ZSM5	Zeolite socony mobil-5

H ₂	Hydrogen
He	Helium
HMF	Hydroxymethylfurfural
HP-INNOWAX	Polyethylene glycol (PEG) based GC column
HP-PLOT/Q	Polystyrene-divinylbenzene (DVB) based GC column
HPA	4-hydroxypentenoic acid
ID	Inner diameter
IHDI	Inequality-adjusted Human Development Index
IPA	Isopropylamine
k_B	Boltzmann constant
k_f	Apparent forward rate constant
kW	Kilowatt
LA	Levulinic acid
LD ₅₀	Lethal dose, 50%
LHS	Left hand side
MFI	Type of zeolite
mL	millimeter
MTHF	Methyl tetrahydrofuran
N	Avogadro's constant
N ₂	Nitrogen
Nb ₂ O ₅	Niobium pentoxide
NO ₂	Nitrogen dioxide
Pd/C	Palladium on carbon

PEA	Pentenoic acid
PFR	Plug flow reactor
PID	Proportional-integral-derivative
ppm	Parts per million
PWA	Phosphotungstic acid
Q	Volumetric flow rate
R	Gas constant
RCR	Ring closure rate
RHS	Right hand side
ROR	Ring opening rate
Ru/C	Ruthenium on carbon
SBP	2-sec-butyl-phenol
sccm	Standard cubic centimeter per minute
SIAL	Silica alumina
SiO ₂	Silica
Sn	Tin metal
SO ₂	Sulfur dioxide
T	Absolute temperature
TCD	Thermal conductivity detector
TFA	Trifluoromethanesulfonic acid
TOF	Turn over frequency
TPD	Temperature programmed desorption
TPPTS	Tris(3-sulfonatophenyl)phosphine

TW	Terawatt
UV	Ultra Violet
WHSV	Weight hourly space velocity
y_j	Mole fraction of species j
ZrO ₂	Zirconium dioxide
γ -Al ₂ O ₃	Gamma alumina
ΔG	Gibbs free energy
ΔH	Enthalpy change of reaction
ΔS	Entropy change of reaction
ε	Extent of reaction
τ	Space time

CHAPTER I

INTRODUCTION

Worldwide the majority of energy consumed by human beings for transportation, agricultural, industrial, residential, commercial and institutional purposes, comes from fossil resources, which are nonrenewable, and their continued use impacts dire consequences on the environment.¹ Currently, global energy production stands at 16 terawatt (TW), and global population is expected to reach 8 billion by 2025.^{1a} The Inequality-adjusted Human Development Index (IHDI), which is a metric of the average level of human development, estimates an average energy consumption of 4 kW/person, for a sustainable life style.² At an average energy consumption rate of 4 kW/person, global energy consumption will double to about 32 TW by the year 2025, necessitating the need for an increase in energy production.

The extraction and combustion of fossil resources for energy services result to the release of carbon dioxide (CO₂), nitrogen dioxide (NO₂), and sulfur dioxide (SO₂).³ The emission of NO₂ and SO₂ into the atmosphere favors the formation of acid rain as these gases combine with attendant water moisture to form nitric acid and sulfuric acid, respectively.³ Acid rain increases the pH of surface water, soils, and clouds leading to adverse effects on aquatic life, microbes, and human health.³ In addition, CO₂ is a green house gas and when released into the atmosphere, absorbs infrared radiation contributing to global warming. According to the Presidential Climate Action Project,⁴ the allowable concentration of carbon dioxide in the atmosphere is 450 parts per million (ppm), and based on current consumption trends, that threshold will be surpassed by the year 2040 unless dependence on fossil energy resources is curtailed.

Fossil energy resources are limited and in decline, and they are prone to price fluctuations, determined not just by demand and supply but also by politics, geographical

location, refining capability and environmental considerations. More so, unless alternative renewable energy sources are explored; with fossil energy resources in decline and an ever-increasing need for energy services, the cost of extracting energy from fossil resources will continue to increase, even with the advent of improved recovery technologies. Although energy production from fossil resources can be improved by targeting more abundant and less expensive fossil resources like coal and natural gas; global energy production from fossil resources using conventional inexpensive technologies has remained around at 4,000 million metric tons per year, and has not changed within the last decade.^{1a} To increase global energy production in a sustainable fashion that meets base consumption mandates (4 kW/person), it's essential to increase energy efficiency alongside employing alternative renewable energy resources that are capable to generate multi-terawatts of energy.

Energy is consumed via energy services and in broad terms, energy services can be divided into two main categories: stationary energy services and mobile energy services. While stationary energy services including heating, cooling and lighting are likely to be met by electricity generated from renewable resources such as solar, wind, nuclear, tidal, biomass, hydro and geothermal; mobile energy services depend heavily on liquid hydrocarbon fuels, which are primarily obtained from fossil resources. Notably, renewable electricity can also be used to provide mobile energy services such as personal transportation (evident by personal electric cars, transit buses and ambulances); however, without significant changes to existing infrastructure, major transportation sectors like aviation and ocean shipping will continue to depend on fossil resources. Even so, changes to existing infrastructure are expensive and will need a considerable length of time to be fully optimized. To that effect, viable and economical conversion of renewable resources into hydrocarbon transportation fuels appears to be a more immediate

remedy and an exciting challenge to tackle, as it will not require any modifications in structure or design of existing internal combustion engines.

Besides the transportation sector, fossil resources constitute the backbone of the chemical manufacturing industry as hydrocarbons derived from fossil resources are utilized as carbon feedstock for the production of specialty chemicals, polymers, and solvents.^{1a, 5} Conceptually, carbon formerly sequestered underground is converted to stable valued-added products, and in the process CO₂ released during combustion of fossil fuels is emitted into the atmosphere (Figure 1). The forfeiture of CO₂ into the atmosphere introduces a carbon imbalance rendering the overall cycle not carbon neutral, and as mentioned earlier, contributes to a net increase of greenhouse gases, which leads to global warming.³ To lessen the dependence of the transportation and chemical manufacturing sectors on fossil resources, as well as mitigate ensuing environmental consequences, alternative renewable carbon sources like biomass, which affords a neutral carbon cycle (because CO₂ produced is recycled via photosynthesis) and upon combustion produces fewer nitrogen oxides and sulfur oxides relative to fossil resources, are essential for clean and sustainable production of energy, transportation fuels, and specialty chemicals.⁶

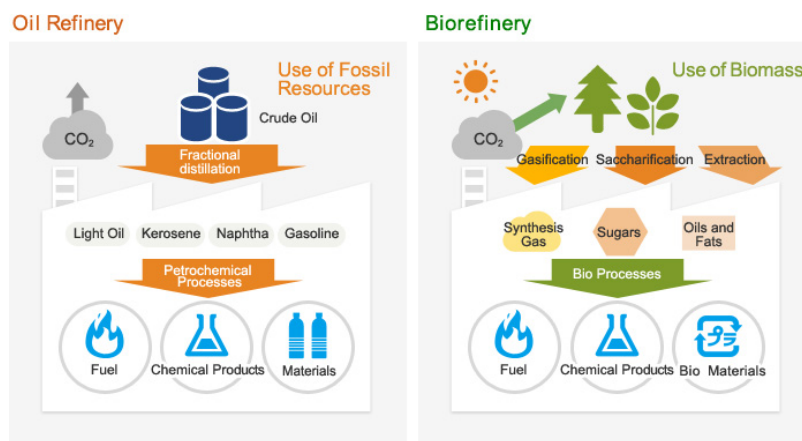


Figure 1. Carbon cycles for petroleum- and bio-refinery.

Biomass feedstock suitable for the production of transportation fuels and specialty chemicals can be classified into three categories: starches, triglycerides, and lignocellulose (Figure 2).⁷ Starchy feedstock comprises of polysaccharides formed from glucose monomers linked by α -glycosidic bonds, which can be easily hydrolyzed by amylase enzymes and dilute acids to form constituent monomeric sugars that are further upgraded to high-value chemicals. Triglyceride feedstock, which can be obtained from plant and animal sources (vegetable oils, algae and animal fats), comprise of esters formed from glycerol and long fatty acid chains that are structurally and compositionally suitable for the production of biodiesel and diesel fuel. Unlike starchy and triglyceride feedstock, which occasionally are obtained from edible starches and oils, compete with food for production, and are only present in select plants and/or crops; lignocellulose feedstock is non-edible and is present in every plant, making it the most abundant and least expensive type of biomass feedstock. The US Department of Energy estimates that lignocellulosic biomass can be produced at \$44 to \$66/dry m.t. at the farm gate and, using its heat of combustion of 18 MJ/kg, translates to an energy cost of \$2.5 to \$3.70/GJ, which is comparable to that of coal and natural gas.⁸

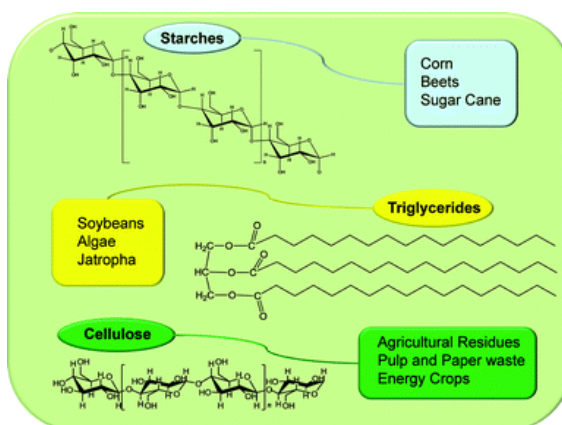


Figure 2. Structural composition of biomass feedstocks (copied from ref 6b).

Lignocellulosic biomass is a mixture of cellulose (40-50%), hemicellulose (25-35%) and lignin (15-20%).⁹ Cellulose is a polymer composed of glucose monomers linked by β -glycosidic bonds.¹⁰ The presence of intramolecular- and intermolecular hydrogen bonding between the polymer chains results in the formation of long fibers, which confer strength and rigidity to plants. Hemicellulose is an amorphous polymer composed of five-carbon and six-carbon sugar monomers, namely: arabinose, galactose, glucose, mannose and xylose, of which xylose is the most prevalent monomer.^{6b, 11} Lignin is an amorphous polymer composed of three main aromatic precursors:¹² *p*-coumaryl-, coniferyl-, and sinapyl alcohols. Unlike cellulose and hemicellulose, the structure of lignin varies with the source of biomass (softwood or hardwood), is non-uniform and is much more complex, making it more difficult to convert to fuels and chemicals.^{5b, 12-13}

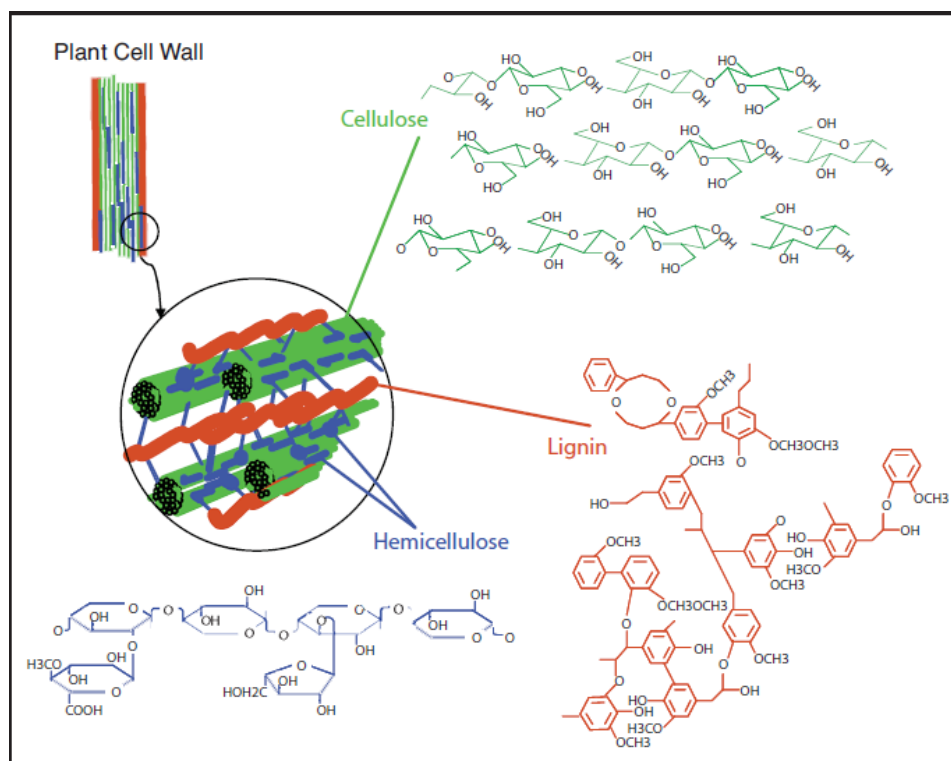


Figure 3. Composition of lignocellulosic biomass (adopted from ref 9).

To ward off predators and microorganisms from consuming attendant sugars in cellulose and hemicellulose, plants inherently possess a defense mechanism that makes it difficult to break down lignocellulose, responsible for rigidity and strength. The difficulty associated with breaking down lignocellulose into constituent sugar monomers, ensures that lignocellulosic biomass can survive a variety of climates and soils around the world, justifying its abundance.^{7b}

¹⁴ Although recalcitrance to breakdown is crucial for the availability of lignocellulosic biomass, it adds to the complexity and challenges associated with converting it to fuels and valued-added chemicals; as it must be pretreated to expose the reactive attendant sugar monomers.^{9, 14b}

Lignocellulosic biomass is a densely oxygenated and highly functionalized feedstock. The main objective in upgrading lignocellulosic biomass to transportation fuels and chemicals is to progressively reduce the high oxygen content of the feedstock to produce a stable platform molecule, with sufficient functionality, that can be further processed to fuels and chemicals.^{11a, 15} For the production of transportation fuels, the goal is to obtain a molecule that has a high energy density, reduced functionality, and good combustion properties. Typically, that entails subjecting the platform molecule to C-C coupling reactions to produce a hydrocarbon with the appropriate molecular weight and energy properties.^{5d, 6b}

In general, the conversion of lignocellulosic biomass to chemicals and fuels is achieved by two processing platforms (Figure 4): biochemical conversion platform and thermochemical conversion platform.^{5b, 5d, 6a, 16} Biochemical conversion encompasses the use of biological enzymes, as well as hydrolysis pathways that selectively fractionate the components of lignocellulose into its constituent sugar monomers (6- and 5-carbon sugars) and lignin.^{5b, 5d, 6a, 16-}

¹⁷ The highly functionalized and more reactive sugar monomers can then be further progressively deoxygenated at mild conditions to obtain intermediate upgradable platform molecules.

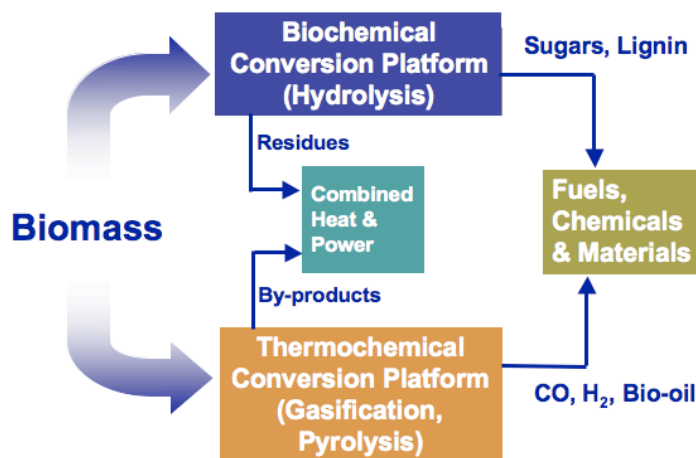


Figure 4. Lignocellulosic biomass processing platforms (adopted from ref 11a).

On the other hand, thermochemical pathways consist of single-step methods that use high temperatures and pressures to deconstruct lignocellulosic biomass, without prior pretreatment steps like drying and down-sizing. These include pyrolysis, gasification and liquefaction. Gasification consists of the partial combustion of biomass to form synthesis gas (CO and H₂ gas mixtures) or producer gas (CO₂, CH₄ and N₂ gas mixtures), which can be further upgraded to liquid fuels or specialty chemicals.^{7a, 18} Pyrolysis refers to the thermal, anaerobic deconstruction of biomass to form bio-oils.¹⁹ To limit the formation of solid coke and also increase bio-oil yields, operations are typically performed at short residence times (seconds). Liquefaction refers to thermal depolymerization of biomass to form bio-oils.¹⁸ Occasionally, homogeneous or heterogeneous catalysts may be employed to increase the quality and yield of the bio-oil. Unlike with pyrolysis, for liquefaction, operations are performed at high pressures and at longer residence times. Bio-oils contain upwards of 350 compounds and are usually reactive, making it difficult and costly to selectively separate and upgrade to a targeted platform molecule or fuel.¹⁸

In comparison, biochemical conversion of lignocellulose is more complex and expensive than thermochemical conversion, and is more applicable for selectively upgrading to targeted intermediate platform molecule.

An important objective in the conversion of lignocellulosic biomass to fuels and chemicals is to limit and/or avoid the introduction of molecular hydrogen gas from external sources.²⁰ Although initial deconstruction steps like pyrolysis, gasification, liquefaction and hydrolysis can be accomplished without the use of hydrogen gas; production of liquid hydrocarbon fuels from intermediate platform molecules usually requires significant amounts of hydrogen gas.^{15, 21} Normally, hydrogen gas is produced by steam reforming of natural gas, which is an energy-intensive and a fossil-resource-based process.²² Hence the use of external hydrogen from fossil resources for biomass conversion limits sustainability and net environmental benefits of the process. One possible solution has been to generate hydrogen gas *in situ*, and then couple reactions that need hydrogen gas with those producing hydrogen gas.²³

CHAPTER II

LITERATURE REVIEW

2.1. Structure and properties of γ -valerolactone (GVL)

GVL is a chiral, 5-membered ring, cyclic ester with molecular formula $C_5H_8O_2$ (Figure 5). Although being a chiral molecule, GVL is commonly used as a racemate. At ambient temperature and pressure, it is a colorless liquid, with a sweet herbaceous odor, and has a high boiling point of 207-208 °C. It is flammable, highly soluble in water, has a low-toxicity (LD50 Oral rat = 8800 mg/kg), and can be stored for extended periods without decomposition.



Figure 5. Molecular structure of GVL.

Despite the simple molecular structure, GVL can be used for a wide range of applications, on account of its renewability, stability, biodegradability and low toxicity. These properties make it possible for GVL to be used as a food additive,²⁴ fuel additive,²⁵ green solvent,²⁶ perfume additive,²⁶ nylon precursor,²⁷ and intermediate platform molecule for producing chemicals and hydrocarbon fuels.^{25, 28} A common risk associated with the general applicability of GVL is its high flammability,²⁹ however, due to its high boiling point and low vapor pressure at ambient temperature and pressure, the risk is much reduced.

Table 1. Physical and chemical properties of GVL^{25, 29}

Property	Value
CAS-No	108-29-2
Formula	C ₅ H ₈ O ₂
Molecular Weight (g mol ⁻¹)	100.112
Refractive index (n ₂₀ /D)	1.432
Density (g ml ⁻¹)	1.05
Flash point (°C)	96
Melting point (°C)	-31
Boiling point (°C)	207-208
Solubility in water (%)	100
ΔH_{vap} (kJ mol ⁻¹)	54.8
$\Delta_c H^{\circ}_{\text{liquid}}$ (kJ mol ⁻¹)	-2649.6±0.8
LD ₅₀ , oral for rat (mg/kg)	8800
Kinematic viscosity (mm ² /s) (40 °C)	2.1
$\Delta_f H^{\circ}_{298}$ (kJ mol ⁻¹)	-461.3
Cetane number	< 10
Lower heating value (MJ/kg)	25

2.2. Production of GVL from lignocellulose biomass

Targeted production of GVL from lignocellulosic biomass can be attained by hydrogenation of levulinic acid (LA).^{11a, 30} Back in 2004, the US Department of Energy recommended LA as a bio-based platform molecule that could be converted to high-value derivatives, thereby improving the overall economy of biomass processing.^{11a, 30a, 31} In principle, LA can be produced from both cellulose and hemicellulose (Figure 6). When subjected to acid hydrolysis, cellulose and hemicellulose degrade into their constituent hexose- and pentose

monomers, respectively.^{9, 32} The hexose monomers upon further acid hydrolysis form intermediate hydroxymethylfurfural (HMF).^{11b, 33} HMF can still further degrade upon acid hydrolysis in the presence of water to form LA.³³ The pentose monomers upon acid treatment form furfural. The resulting furfural can be hydrogenated to produce furfuryl alcohol,³⁴ which upon acid treatment results to the formation of LA. Furfuryl alcohol and LA can still be further esterified, using ethanol, to produce ethyl levulinate,³⁵ which upon hydrogenation forms GVL.³⁶

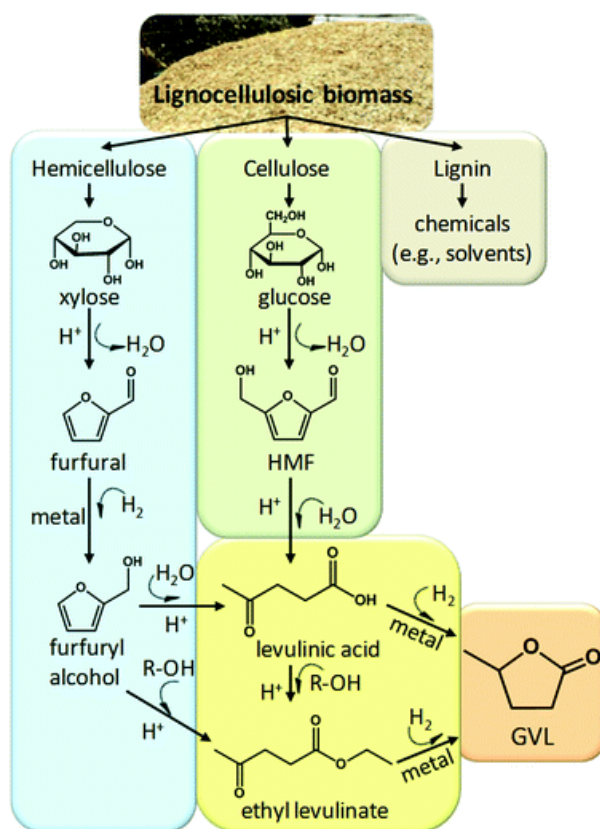


Figure 6. Production of GVL from lignocellulosic biomass (copied from ref 37).

The hydrogenation of LA to produce GVL is challenging and a lot of the difficulty stems from the entrainment of mineral acids, which poisons catalysts as well as makes separation steps difficult thereby increasing the overall cost of converting LA to GVL. The most common

mineral acid used for deconstruction of lignocellulose and subsequent hydrolysis steps to form LA is sulfuric acid. The propensity of sulfur atoms to adsorb on catalyst supports means that entrained sulfuric acid poisons hydrogenation catalysts.^{5d, 37} Most heterogeneous catalysts for LA hydrogenation to GVL are Ru-based. Manzer et al³⁸ and Liu et al³⁹ have independently demonstrated that GVL can be obtained from LA in quantitative yields and selectivity using Ru/C catalyst. However, Ru is a noble metal and Ru/C is easily poisoned by entrained sulfuric acid used in the production of LA,^{5d, 37} necessitating the need for noble-metal-free catalysts that can effect hydrogenation of LA to GVL. In that respect, Hengne et al⁴⁰ have reported quantitative yields of GVL from LA over nano-composites of Cu-ZrO₂ and Cu-Al₂O₃, in the liquid phase. The authors suggest that the acidity of the catalyst supports (ZrO₂ and Al₂O₃) favors the cyclization of intermediate HPA to GVL. Although these results were obtained at high temperatures and hydrogen pressures, they indicate that hydrogenation is possible with inexpensive catalysts. Still, further optimization is necessary, but the introduction of such catalysts will help reduce overall manufacturing cost of GVL from LA.

Another challenge associated with converting LA to GVL relates to the use of external sources of molecular hydrogen. As noted in the previous chapter, the use of fossil-based hydrogen to effect hydrogenation of LA to GVL reduces sustainability and net environmental gains of the process. To curtail the dependence on external molecular hydrogen, Deng et al.^{31a} have reported a method, which leverages a byproduct of LA production, formic acid (FA), to generate hydrogen *in situ* for the hydrogenation of LA. As an additional bonus, this method eliminates separations steps required to separate LA from FA, which improves the overall economy and also reduces manufacturing costs for the process. Although the mechanism by which hydrogen is generated is still not well established, FA either decomposes directly to form

molecular hydrogen and CO₂, or, it reacts to form a metal-formate, which upon decomposition produces a metal hydride and CO₂. In the former approach, the resulting molecular hydrogen hydrogenates LA to GVL, while in the latter approach, the metal hydride converts LA to 4-hydroxypentenoic acid (HPA), which rapidly cyclizes by lactonization to form GVL.

To improve the economy and energy efficiency of heterogeneous hydrogenation of LA to GVL, efforts have been directed at producing GVL at relatively mild conditions by introducing acid co-catalysts. Galletti et al⁴¹ have demonstrated improved hydrogenation of LA to GVL under mild conditions using Ru/C catalyst and Amberlyst 70 as co-catalyst. Operating at 70 °C, 0.5 MPa of H₂, for 3 h in water, the yield to GVL was reported at 99.9%. At the same reaction conditions, in the absence of the Amberlyst 70 acid co-catalyst, LA conversion of only 13% was measured. Similarly, acidic co-catalysts and supports have also been used to catalyze the cyclization of HPA acid through lactonization to GVL under relatively mild conditions. For instance, Mondo et al⁴² used a 316 stainless steel catalyst in the presence of trifluoromethanesulfonic acid as a co-catalyst, at 75 °C, to completely convert HPA to GVL. Apparently, acidic co-catalysts and supports must be selected carefully to avoid acid-catalyzed ring opening of the resulting GVL to 4-pentenoic acid, and other related compounds like 1,4-pentanediol and methyl tetrahydrofuran (MTHF).^{30c, 42}

To minimize processing steps as well as the overall manufacturing costs pertaining to hydrogenation of LA to GVL, one pot processes which target the direct conversion of biomass to GVL have also been explored. The advantage is to eliminate separation costs and processing steps associated with isolating intermediate LA. These one pot processes rely on tandem catalysis and require the combination of both a biomass deconstruction catalyst and a hydrogenation catalyst. Mehdi et al⁴³ have reported a tandem system consisting of various

homogenous and heterogeneous catalysts to convert sucrose into GVL. The cascade is initiated by acid-catalyzed dehydration of sucrose with either sulfuric acid or Nafion-NR50, to form LA and FA. The FA serves as a hydrogen source for the hydrogenation of LA to GVL over Ru(acac)₃ and tris-(3-sulfonatophenyl)phosphine (TPPTS). Although the GVL is not directly derived from a biomass feedstock, introduction of the concept of tandem catalysis to GVL production from biomass is essential for the development of an integrated process. Heeres et al⁴⁴ have reported a similar tandem catalytic system which combines homogeneous acid dehydration and heterogeneous hydrogenation catalysts. The acid dehydration catalyst must be selected carefully as conventional mineral catalysts like sulfuric acid poisoned the hydrogenation catalysts. The authors found trifluoroacetic acid (TFA) capable of producing LA without hindering the ensuing hydrogenation step catalyzed by Ru/C. The resulting tandem catalysis system was used to convert fructose into GVL in the presence of molecular hydrogen with a yield of 52% at 180 °C. In the presence of molecular hydrogen, using glucose as a feedstock, the yield to GVL of 46% was reported. Control experiments in the absence of molecular hydrogen resulted in lower yields to GVL, implying less efficient conversion of glucose and Fructose to LA.

Multiphase systems have also been developed to facilitate the separation of products and catalysts during hydrogenation of LA to GVL. Bourne et al⁴⁵ have introduced a liquid phase system consisting of supercritical CO₂ and water for the production of GVL from LA. Upon formation, GVL is immediately taken up into supercritical CO₂, where it is obtained in an almost pure state after separation and pressure relieving of supercritical CO₂. In the aqueous phase, using a Ru/SiO₂ catalyst the authors reported 99% yield of GVL from LA. Similarly, Dumesic et al⁴⁶ have reported a biphasic system consisting of water and 2-sec-butyl-phenol (SBP) for hydrogenating LA to GVL using RuSn bimetallic catalysts. In principle, the high partition

coefficient of GVL between water and SBP ensures that GVL is taken up into SBP. In this system, SBP is considered a renewable solvent that can be produced from lignin and the inclusion of Sn prevented the formation of hydrogenation products from the solvent.

2.3. Derivatives of γ -valerolactone

Despite the simple molecular structure, GVL has a wide range of applications thanks to its reactivity, stability, low toxicity and renewability, which make it a platform molecule suitable for upgrading to high-value chemicals and hydrocarbon fuels.^{15, 26, 38, 47} In its pure form, GVL can be used as a food additive,²⁴ fuel additive,²⁵ perfume additive²⁶ and as a green solvent.²⁶ Figure 7 illustrates high-value chemicals and hydrocarbon fuels that can be derived from GVL.

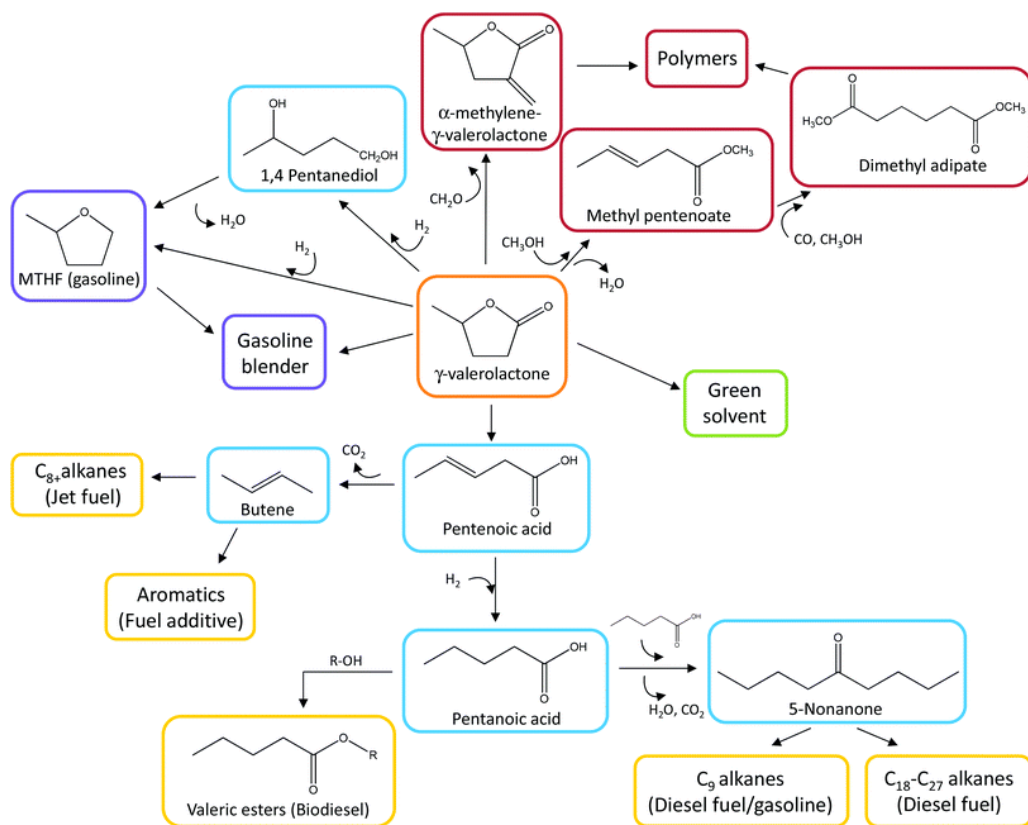


Figure 7. Schematic of high-value derivatives from GVL (copied from ref 49a).

In addition to standalone uses, GVL can be converted to produce polymer precursors.²⁷ Notably, GVL undergoes acid-catalyzed transesterification in the presence of methanol, at elevated temperatures (400 °C) to form methyl pentanoate, which can further react through hydroformylation, hydrocyanation, or hydroxycarbonylation to produce nylon precursors caprolactone, caprolactam, or adipic acid, respectively. Similarly, GVL can react with formaldehyde to form α -methylene- γ -valerolactone,³⁸ a precursor for acrylate polymers, with potential to improve thermal resistance in the end polymer.

Besides the production of polymer precursors, GVL can be hydrogenated to form methyl tetrahydrofuran (MTHF),⁴⁸ a P-series fuel that can be blended up to 70% by volume with gasoline for use in current transportation infrastructure. The reaction entails hydrogenating GVL to 1,4-pentanediol followed by dehydration to form MTHF. Another important application of GVL is for production of hydrocarbon fuels (jet fuel, gasoline and diesel).⁴⁹ First, GVL undergoes ring opening to form pentenoic acid isomers followed by hydrogenation over Pd/Nb₂O₅ catalyst to form pentanoic acid.^{49a} In principle, acid sites on the niobia (Nb₂O₅) support are responsible for ring opening while Pd metal sites effect hydrogenation of the resulting pentenoic acids to pentanoic acid. The use of the bifunctional catalyst ensures that the rate of decarboxylation is slow relative to hydrogenation making it possible for resulting pentenoic acid isomers to be hydrogenated to pentanoic acid. The resulting pentanoic acid can be upgraded to 5-nonanone by ketonization over niobia and/or ceria-zirconia catalysts.⁵⁰ The 5-nonanone can then be hydrogenated directly to form C₉ alkanes that can be blended in diesel fuel, or, hydrogenated initially to 5-nonanol followed by dehydration to form nonene isomers, which undergo oligomerization followed by subsequent hydrogenation to form C₉-C₁₈ alkenes.⁵¹

In the absence of metal-catalyzed hydrogenation, GVL can ring open over a solid acid catalyst like $\text{SiO}_2/\text{Al}_2\text{O}_3$ to form intermediate pentenoic acid isomers which decarboxylate to form butene and CO_2 in equal mole ratios.⁵² Through C-C coupling reactions over H-ZSM5 or Amberlyst-70, the resulting butenes can be upgraded to higher range alkenes suitable for production of jet fuels. As the concentration of the CO_2 stream produced is high, it can be easily sequestered or leveraged for other processes. The benefits of combining the decarboxylation and oligomerization steps sequentially has been demonstrated by Bond et al^{49a} in an integrated process for converting GVL to liquid alkenes. As discussed earlier in the chapter, hydrogen management is an important objective in upgrading biomass to liquid hydrocarbons. Combining the decarboxylation and oligomerization steps completely eliminates the need for an external source of hydrogen and carbon dioxide emission. In principle, the ring-opening step is independent of hydrogen while subsequent oligomerization and hydrogenation steps require molecular hydrogen. Bond et al,^{49a} report that as the extent of oligomerization increases, the need for hydrogen decreases, thus eliminating the requirement for external hydrogen.

2.4 Decarboxylation of GVL

2.4.1 Mechanism of GVL decarboxylation

The first step in the decarboxylation of GVL is the acid-catalyzed ring opening of the lactone to form isomers of PEA. This is followed by decarboxylation of the PEA isomers to form butene isomers and CO_2 . In a recent combined computational and experimental study, Bond et al⁵³ investigated the thermodynamics of the initial ring opening and subsequent decarboxylation steps. Using Gaussian 03 software,⁵⁴ the enthalpy changes for ring opening of GVL to PEA isomers at 298 K were estimated to be 17, 25, 26, 32, and 36 kJ mol^{-1} for *trans*-2-PEA, *trans*-3-

PEA, *cis*-2-PEA, *cis*-3-PEA and 4-PEA, respectively. This implies that at room temperature the formation of PEA isomers is unfavorable. Similarly, the changes in Gibbs free energy at 298 K were estimated at 25, 8, 14, 16 and 19 kJ mol⁻¹ for 4-PEA, *trans*-2-PEA, *trans*-3-PEA, *cis*-2-PEA and *cis*-3-PEA, respectively. The changes in entropy at 298 K were 37, 37, 44, 30, and 34 J/mol/K for 4-PEA, *trans*-3-PEA, *cis*-3-PEA, *trans*-2-PEA and *cis*-2-PEA, respectively. This implies that ring opening to PEA isomers is favored entropically. Overall, from their calculations, the ring-opening step at room temperature is endothermic, non-spontaneous, and unfavorable. Utilizing an average distribution of isomers, entropy, enthalpy and Gibbs free energy changes at 298 K were estimated for the decarboxylation step at 148 J/mol/K, -49 kJ mol⁻¹ and -93 kJ mol⁻¹, respectively. This means that at room temperature, decarboxylation of PEA isomers is exothermic, irreversible, and is favored entropically. Drawing from these calculations, the overall changes in enthalpy and Gibbs free energy for the conversion of GVL to butenes and CO₂ were estimated to be 22 kJ mol⁻¹ and -77 kJ mol⁻¹, respectively.

Bond et al⁵³ have investigated the extent to which PEA contributes to decarboxylation. By co-feeding GVL and H₂ over a bed of catalyst consisting of SiO₂/Al₂O₃ and Pd/C, the production of CO₂ was heavily suppressed as PEA formed was immediately hydrogenated to pentanoic acid. From that observation, the authors concluded that PEA is an intermediate in the decarboxylation pathway, and the presence of the double bond is critical for decarboxylation. By subjecting a series of saturated and unsaturated acids to decarboxylation conditions, Bond et al⁵³ further observed that the unsaturated acids underwent decarboxylation, while the saturated ones did not, confirming that PEA is a key contributor in the decarboxylation event. In the same study, the unsaturated acids produced GVL as a byproduct, indicating that the ring-opening step is reversible. This was further corroborated by the observation of equilibrium ratios of GVL and

PEA at long space times, implying that the interconversion between GVL and PEA is rapid at reaction conditions and is reversible. The length of the PEA intermediate was also found to have an effect on decarboxylation. When acrylic acid was subjected to decarboxylation conditions, insignificant extent of decarboxylation ($< 1 \mu\text{mol/g/min}$) was observed, implying that the double bond situated at the α -position does not favor the formation a stable protonated intermediate. Through further screening, the authors concluded that for decarboxylation to occur, the possibility must exist for a C=C double bond that can be protonated to form a secondary carbenium ion at the β -position to the carboxylic acid group. Bond et al⁵³ also estimated the apparent activation barriers for ring opening and ring closure to be $85 \pm 19 \text{ kJ/mol}$ and $59 \pm 24 \text{ kJ/mol}$, confirming that ring-opening of GVL is less favored compared to ring closure.

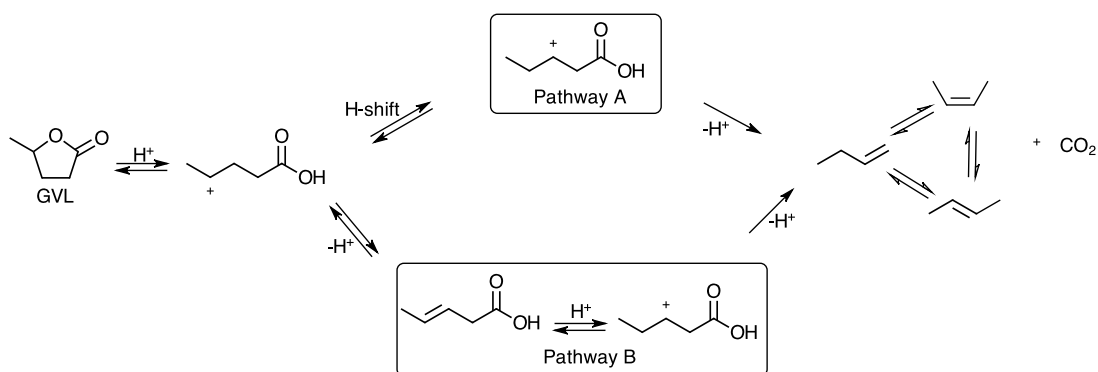


Figure 8. GVL decarboxylation pathways.

Drawing from the above discussion, Bond et al⁵³ suggested two pathways for decarboxylation of GVL over solid acids (Figure 8). Both pathways begin with the acid-catalyzed ring opening of the lactone to form an intermediate carbenium ion (charge on γ -carbon from acid group). The resulting carbenium ion can then react through Pathway A or Pathway B to form butenes and CO_2 . Through a series of experiments involving saturated and unsaturated

acids, Pathway B was suggested to be the lower energy route.⁵³ For pathway A, the intermediate carbenium ion undergoes a series of hydride shifts, eventually forming the carbenium ion with the charge at the β -carbon, which decarboxylates to produce butenes and CO₂.

In a follow up study reported by Bond et al,⁵² the activation barriers of pathways A and B were estimated to be 175 ± 20 kJ/mol and 142 ± 11 kJ/mol, respectively, confirming that indeed Pathway B is the preferred route to decarboxylation. It was further estimated that Pathway A contributes about 10-20% of the overall butene production rate, while the balance is from Pathway B. In the same study,⁵² the authors observed that the distribution of butene isomers varied with space time. At shorter space times, 1-butene was the major product, while at longer space times, *cis*-2-butene and *trans*-2-butene were dominant, indicating that 1-butene is initially formed by cleavage of the bond between the α -carbon and carbonyl group. Through isomerization, the other butene isomers are formed from 1-butene. This observation is consistent with the initially proposed mechanism for decarboxylation.

2.4.2. Kinetics of decarboxylation of GVL

Bond et al⁵² have developed a semi-empirical model for decarboxylation of GVL over SiO₂/Al₂O₃ to produce butenes and CO₂. The kinetic model takes into account that decarboxylation either occurs directly from GVL or proceeds through intermediate PEA isomers. To construct the model, apparent reaction orders of GVL, PEA, and water were estimated by investigating the dependence of the rates of ring opening and decarboxylation on the partial pressure of each species. Both GVL and PEA revealed positive fractional order dependence on the rates of ring opening and ring closure, respectively, as well as for decarboxylation. For GVL, apparent reaction orders were estimated to be 0.16 ± 0.03 for ring opening and 0.45 ± 0.09 for

decarboxylation. Basically, increasing the partial pressure of GVL has little effect on the rates of ring opening and decarboxylation, suggesting a strong interaction between GVL and the $\text{SiO}_2/\text{Al}_2\text{O}_3$ surface that leads to saturation of acid sites at high GVL partial pressure, limiting the response to rates for further increases in GVL partial pressure. Similarly, for PEA the apparent reaction order for ring closure and decarboxylation were estimated to be 0.37 ± 0.07 and 0.31 ± 0.07 , respectively. The similarity in reaction orders for PEA was suggested to mean that a unimolecular reaction was involved on the surface. Bond et al⁵² further estimated apparent reaction orders of ring opening and decarboxylation, with respect to water. For both ring opening and decarboxylation, water was found to have negative apparent reaction orders, estimated at -0.65 ± 0.2 and -0.85 ± 0.45 , respectively. This observation suggests that water competes with GVL for acid sites on the surface of $\text{SiO}_2/\text{Al}_2\text{O}_3$. From the apparent reaction orders, it is evident that GVL, PEA and water all interact with the catalyst surface, as such were included in the rate equations of the semi-empirical model. Because experiments were performed at high temperatures and at low extent of reaction, leading to low partial pressures of butene, mostly 1-butene was observed without isomerization or oligomerization products, indicating little interaction with the catalyst. Hence, adsorption of butene does not compete with that of GVL, PEA or water, justifying its exclusion from the governing rate equations by the authors.

The semi-empirical model reported, assumes a unimolecular surface reaction for all surface reactions and, to meaningful describe experimental data, a two site-blocking term was used in the denominator of the surface coverage expression (Equation 4) implying that two different sites may be involved in the reaction. The main equations used for the construction of the semi-empirical model are:

$$1. \quad r_1 = k_1 \theta_{GVL} - k_{-1} \theta_{PEA} \quad \text{Equation 1}$$

$$2. \quad r_2 = k_2 \theta_{GVL} \quad \text{Equation 2}$$

$$3. \quad r_3 = k_3 \theta_{PEA} \quad \text{Equation 3}$$

$$4. \quad \theta_i = \frac{K_i P_i}{((1+K_{GVL} P_{GVL} + K_{PEA} P_{PEA}))^m (1+K_{H_2O} P_{H_2O})^n} \quad \text{Equation 4}$$

$$5. \quad k_i = k_{0_i} e^{\left(\frac{-E_A}{R} \left(\frac{1}{T} - \frac{1}{T_0}\right)\right)} \quad \text{Equation 5}$$

$$6. \quad K_i = K_{0_i} e^{\left(\frac{-\Delta H_{ads}}{R} \left(\frac{1}{T} - \frac{1}{T_0}\right)\right)} \quad \text{Equation 6}$$

2.5. Intrinsic behavior of different solid acids during decarboxylation

Kellicutt et al⁵⁵ have investigated the intrinsic activity and stability of different solid acids during decarboxylation of GVL. In their study, four types of materials were screened including amorphous silica alumina (ASA), MFI zeolite, phosphotungstic acid (PWA), and gamma alumina ($\gamma\text{-Al}_2\text{O}_3$). ASA is amorphous, mesoporous and contains both Bronsted sites associated with framework aluminum and Lewis sites associated with extraframework aluminum. MFI zeolite is microporous and exhibits primarily Bronsted acidity. $\gamma\text{-Al}_2\text{O}_3$ is Lewis acidic, while PWA is a supported heteropolyacid that exhibits Bronsted acidity and deprotonates readily. By comparing initial decarboxylation rates (DC) obtained in the gas phase, under differential conditions, Kellicutt et al⁵⁵ examined the roles of Bronsted and Lewis acidity,

deprotonation energy, and catalyst morphology in each catalytic material and how these influenced the intrinsic rate and stability of the catalysts. The authors report that of the materials screened, MFI zeolites is most active towards GVL decarboxylation having initial DC rates ranging from 220-750 $\mu\text{mol min}^{-1} \text{g}^{-1}$ and, for this material DC rates generally increase with aluminum content. ASA is slightly less active than MFI zeolites having initial DC rates ranging from 60-440 $\mu\text{mol min}^{-1} \text{g}^{-1}$; however, no clear correlation could be established between DC rates and aluminum content. PWA and $\gamma\text{-Al}_2\text{O}_3$, are less active than ASA and MFI zeolites, affording initial DC rates of 7.8 and 1.5 $\mu\text{mol min}^{-1} \text{g}^{-1}$, respectively. From these observations, the authors noted that aluminosilicates are well-suited catalysts for GVL decarboxylation and high aluminum content is beneficial for catalyst productivity.

To investigate the intrinsic activity of each material towards GVL decarboxylation, the authors plotted mass-normalized butene production rates against Bronsted site density. In ASA, mass-normalized DC rates show a first order dependence on Bronsted site density, with a reported slope of 0.99 ± 0.21 , implying that the rates depend entirely on Bronsted site density and are kinetically controlled. In addition, the rates do not vary with aluminum content, and an average turn over frequency (TOF) of $1.36 \pm 0.13 \text{ min}^{-1}$ was reported for a Bronsted site in ASA. In $\gamma\text{-Al}_2\text{O}_3$, observed DC activity is attributed to Lewis sites associated with coordinatively unsaturated aluminum sites in the structure and, a TOF of 0.01 min^{-1} was estimated for a Lewis site. In MFI zeolites, internal diffusion controls the rate of decarboxylation at high temperatures and reported TOFs decrease with increasing aluminum content. For instance, at 623 and 523 K, the TOF for a Bronsted site on MFI zeolites is estimated respectively at $0.43 \pm 0.16 \text{ min}^{-1}$ and $0.84 \pm 0.34 \text{ min}^{-1}$. This indicates that DC rates shift towards kinetic control at 523 K, scaling linearly with Bronsted site density. In addition, the authors determined that at low aluminum

content, DC rates scale linearly with Bronsted site density and are kinetically controlled and, to allow meaningful comparisons with ASA, a TOF of $5.54 \pm 0.36 \text{ min}^{-1}$ was estimated for a Bronsted site in MFI zeolite, at 623 K.

To determine the effect of deprotonation energy on observed mass-normalized DC rates, Kellicutt et al⁵⁵ determined TOFs for each material at 623 K and 0.19 bar GVL partial pressure. The estimated TOF were 5.54, 1.36, 0.26, and 0.01 min^{-1} respectively for MFI zeolite, ASA, PWA/SiO₂ and γ -Al₂O₃. Further, respective activation barriers to DC were estimated at 138 ± 13 , 130 ± 24 , 92 ± 10 , and $172 \pm 36 \text{ kJ mol}^{-1}$. Bronsted sites on ASA and MFI zeolites have comparable deprotonation energies, approximately 1200 kJ mol^{-1} , while that of PWA/SiO₂ is between $1050\text{-}1100 \text{ kJ mol}^{-1}$. The deprotonation energies of a Bronsted site and activation barriers to GVL decarboxylation for ASA and MFI zeolites are the same, but their respective TOF are very different. Similarly, lower deprotonation energy for a Bronsted site on PWA/SiO₂ does not translate to a higher TOF. For γ -Al₂O₃ its high activation barrier to GVL decarboxylation is consistent with the low mass-normalized DC rates observed. From these observations, Kellicutt et al⁵⁵ established that a more easily deprotonated site does not necessarily imply a more active catalyst during GVL decarboxylation.

To compare catalytic stability of the materials tested, Kellicutt et al⁵⁵ estimated deactivation constants from respective plots of dimensionless activity versus time on stream, by assuming pseudo-first order behavior at short times on stream. From these analyses, all materials showed a loss in catalytic activity with time on stream, through coke formation. For aluminosilicates, catalytic stability scales with microporosity and average pore diameter, leading to more rapid loss of activity in microporous (MFI zeolites)- than mesoporous (ASA) materials. In addition, multiple ASA samples with varying Bronsted to Lewis site ratios revealed

comparable deactivation profiles, implying that Lewis acidity does not promote coke formation. For materials with pore dimensions that do not influence deactivation kinetics (PWA/SiO₂ and γ -Al₂O₃), a lower Bronsted site deprotonation energy echoes more severe deactivation, indicating that deactivation is more rapid when Bronsted sites are easily deprotonated, during GVL decarboxylation.

Among the materials considered by Kellicutt et al,⁵⁵ aluminosilicates appear to be the most practical class of solid acids for GVL decarboxylation, although pore dimensions appear to influence catalytic activity and stability. Based on their findings, they recommend that the ideal solid acid catalyst for GVL decarboxylation possess an aluminosilicate framework, mesoporous sized pores, a high density of Bronsted sites, and strong acid strength. More specifically, Al-MCM-41, a mesoporous aluminosilicate with strong Bronsted acid sites, which satisfy the aforementioned criteria, is suggested as a probable candidate. However, the observation that ASA and MFI zeolites, even though being aluminosilicates with comparable Bronsted site deprotonation energies and identical experimentally determined apparent activation barriers to decarboxylation, afforded markedly different apparent TOF (four times higher for MFI zeolites) is intriguing. Although this could imply that the local surroundings of the Bronsted site is essential for intrinsic activity of the material towards decarboxylation; it could also point to an elementary surface phenomenon not captured by the lumped apparent activation barriers experimentally determined. One way to ascertain if the observed difference in apparent TOFs is associated with an elementary surface phenomenon would be to develop a microkinetic model, which describes decarboxylation of GVL over a solid acid having an aluminosilicate framework. As described earlier in this chapter, decarboxylation of GVL involves two mechanistic pathways, both originating from a common surface intermediate; the advent of a microkinetic model,

encompassing both mechanistic pathways, will provide insights into the surface phenomena involved at an elementary level. Such information will not just be restricted to addressing the difference in apparent TOFs mentioned above, but will also be beneficial to the development of an active and stable catalyst for GVL decarboxylation. That is, because the basic surface chemistry during GVL decarboxylation is independent of the catalytic material, information from a single amorphous aluminosilicate catalyst will be applicable to related aluminosilicates. In addition, a microkinetic model will substantiate the recommendations by Kellicutt et al for an ideal GVL decarboxylation catalyst.

In this project, our aim is to develop a microkinetic model for decarboxylation of GVL over a mesoporous aluminosilicate. Although Kellicutt et al had identified Al-MCM-41 as a potential material that validates their base recommendations for an ideal catalyst; for this study, ASA was selected for the development of a microkinetic model. As a microkinetic model can be applied to related materials, we found it more convenient to work with ASA since it has already been used for previous studies on GVL decarboxylation. Specifically, DAVICAT SIAL 3113, already used extensively by Bond et al⁵²⁻⁵³ and Kellicutt et al⁵⁵ for GVL decarboxylation, was used for experimental studies pertaining to the development of the microkinetic model.

CHAPTER III

MATERIALS AND METHODS

3.1 Materials

ASA catalyst DAVICAT SIAL 3113, obtained from Grace Davison, was employed as solid acid catalyst. To eliminate residual moisture and improve weighing accuracy, prior to use commercial samples of the catalyst were calcined at 723 K, for 4 h, in a stream of air (50 sccm), at a heating rate of 3 K min⁻¹. Brooks instrument mass flow controllers (model 5850S) were used to control all gas flow rates. Prior to use, γ -valerolactone (GVL, >98%, Sigma-Aldrich) was dried overnight over silica gel (5% w/v, 12-24 mesh, Strem Chemicals) at ambient pressure and temperature. Unless otherwise stated, *trans*-2-pentenoic acid, *trans*-3-pentenoic acid, 4-pentenoic acid, 1-butene (1% in He, Scott), and CO₂ (5% in N₂, Airgas) were used as purchased without further purification, for instrument calibration. Purified water (Type I) used for sample preparation was prepared by sequential reverse osmosis, UV oxidation, and double deionization. Acetone (>98%, ACROS), He (99.999%, Airgas), N₂ (99.999%, Airgas), Air (Medical Grade, Airgas), silica granules (850-2000 μ m, 99.9%, Sigma Aldrich), quartz wool (from Sigma Aldrich), were used for multiple applications (*vide infra*) without further purification.

3.2 Catalyst characterization

All materials were characterized by physisorption of N₂ at 77 K (Micromeritics ASAP 2020). Prior to dosing N₂, samples were evacuated at 363 K and subsequently outgassed under vacuum (623 K, 4 h). Brunauer-Emmett-Teller (BET) theory and *t*-plot analyses were used to determine total and micropore surface areas, respectively. Barrett-Joyner-Halenda (BJH) analysis of the desorption branch of N₂ uptake isotherms were employed for determination of pore

diameters for mesoporous samples.⁵⁶ Pore dimensions for microporous samples were determined using the Saito-Foley modification to the Horvath-Kawazoe method.⁵⁷ Pore volumes were estimated from the cumulative amount of nitrogen uptake at a relative pressure of 0.995.

Bronsted site densities were determined from molar quantities of propylene evolved between 570-870 K during temperature programmed desorption (TPD) of 2-propanamine. Approximately 50-100 mg of powdered catalyst were loaded into a quartz tube (1/2") on top of a quartz wool plug, and the tube positioned in a high temperature furnace (Omega) and connected to a gas flow manifold. Prior to analysis, catalysts were calcined *in situ* at 673 K, for 4 hours, under 50 sccm of air (Airgas, Ultra Zero). Subsequently, the samples were cooled to 423K, purged with 100 sccm of He (Airgas UHP 99.999%) dried over molecular sieves. Upon pretreatment, the samples were held at 423 K and contacted with 2-propanamine (99%, Acros). The cell was then purged with He (423 K, 400 sccm, 60 min) and subsequently ramped to 973 K (10 K min⁻¹). During the temperature ramp, the effluent was monitored using a mass selective detector (Stanford Instruments RGA 100), and signals corresponding to 2-propanamine (m/z = 44) and propylene (m/z = 41) were monitored, continuously. Bronsted site densities were calculated from evolved propylene based on the assumption that one molecule of propylene forms at each accessible Bronsted site.

3.3 Decarboxylation of GVL and PEA over SiO₂/Al₂O₃ (DAVICAT SIAL 3113)

The decarboxylation of GVL and *trans*-2-pentenoic acid over SiO₂/Al₂O₃ was studied in the gas phase using a down configuration fixed bed reactor. The experimental setup used comprises of a liquid-gas contactor, gas mixer, bypass, furnace, liquid-vapor separator and in-line gas chromatograph (Figure 9). The role of each component is highlighted in the discussion following. Importantly, due to the high boiling points (480 K and 460 K for GVL and *trans*-2-

pentenoic acid, respectively) and low vapor pressures of the reactants; except for the liquid–vapor separator, all other components and connections were heat-traced and temperature-regulated right into and out of the gas-sampling valves of the in-line gas chromatograph (GC), and then onto a downstream condenser, where low vapor pressure species condensed while volatile species were retained in the vapor phase in an exhaust stream.

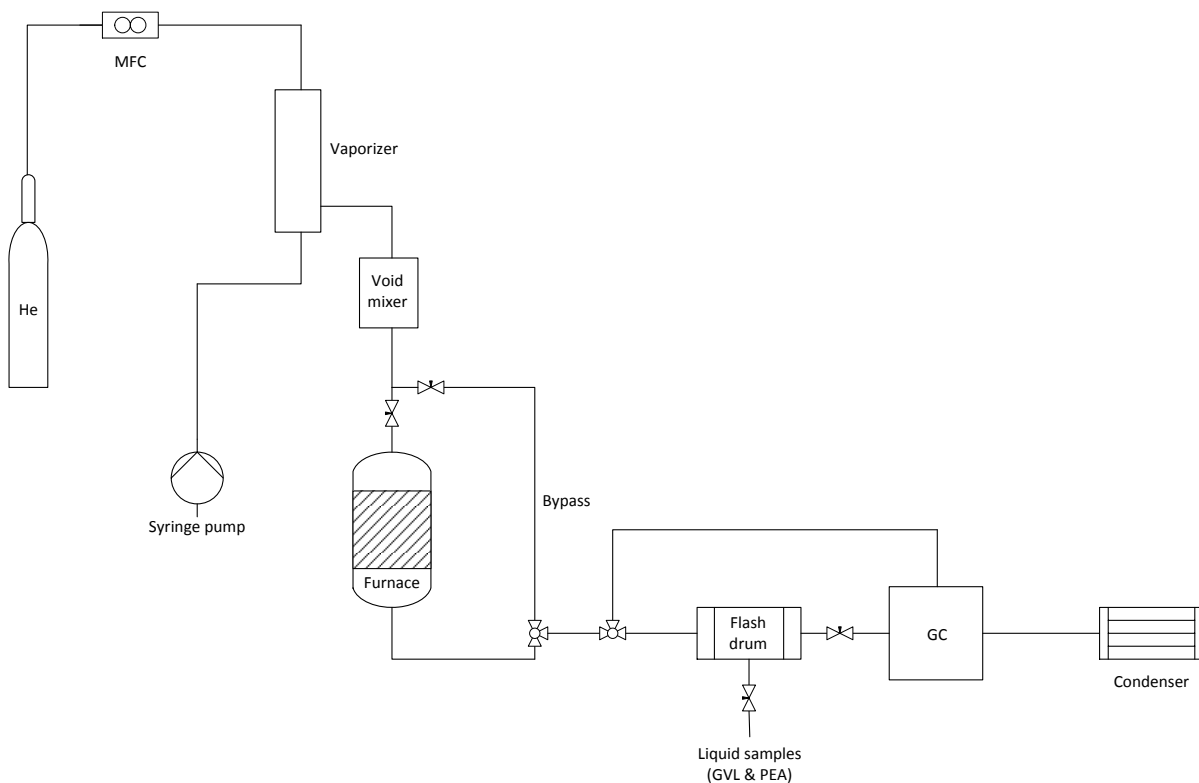


Figure 9. Schematic representation of experimental apparatus.

To minimize pressure differentials across the catalyst bed, catalyst loadings were mixed physically with silica granules (850-2000 μm) and the resulting mixtures loaded into a 316 stainless steel tube with a 1/2" outer diameter. Typically, the “diluted” catalyst bed was 6 inches in length and was suspended between two end plugs of quartz wool. Dead volume upstream of

the catalyst bed was filled with silica granules (850-2000 μm), and the upper end of the reactor tube plugged with quartz wool. On the other hand, dead volume downstream of the catalyst bed was leveraged to position a Type K thermocouple (Omega) in-line to monitor reaction temperature at the bed. The reactor was mounted inside an aluminum block in an insulated furnace. Reactor temperature was controlled using a Type K thermocouple (Omega) regulated by a PID controller (Omega CN7500). The thermocouple was positioned between the reactor and aluminum block, at the same height as that in-line. Preceding the introduction of reactant feeds into the reactor, catalysts were calcined (723 K, 50 sccm, 3 K min^{-1} , 4 h) *in situ* and allowed to attain desired reaction conditions.

Reactant feed (GVL or *trans*-2-pentenoic acid), at ambient pressure and temperature, was introduced into the experimental apparatus using a syringe pump (Cole-Parmer, model 110) fitted with a Hamilton Gas Tight syringe (Series 1000) and stainless steel capillary tube (150 μm ID). The use of the stainless steel capillary tube minimized dead volume between the syringe pump and setup as well as facilitated uniform vaporization of the reactant feed. Typically, reactant feed flow rates ranged from 0.5-32 $\mu\text{l min}^{-1}$ and were selected to attain desired weight hourly space velocities (WHSV). The liquid reactant feed was vaporized in a temperature-regulated liquid-gas contactor upon contact with a hot countercurrent stream of He gas (25-260 sccm), controlled by a mass flow controller (Brooks instrument, Model 5850S). The liquid-gas contactor was equipped with a Type K thermocouple (Omega), positioned in-line at the site of contact, and controlled by a PID controller (Omega CN7500). To prevent liquid feed from boiling in the supply capillary tube, resulting to unsteady vaporization; the temperature of the liquid-gas contactor was always set below the boiling point of the reactant feed. Routinely, the temperature of the liquid-gas contactor was maintained at desired reaction temperature, except

for experiments with reaction temperatures higher than the boiling point of the reactant feed, in which case it was set at 451 K. The combined reactant/He stream from the liquid-gas contactor was then preheated and mixed in a gas mixer downstream prior to being introduced into the reactor.

During operation, the reactor purged with He gas was isolated and flow directed through the bypass until steady concentrations of the reactant were observed from the reactant/He stream, at which point flow was redirected to the reactor inlet. Depending on reaction conditions, the reactor effluent was either sent directly to an in-line GC or detoured to a vapor-liquid separator en route to the in-line gas GC. To ensure that observed GC detector responses were within mandated precision range, reactor effluent streams with high concentrations of species (> 20 mbar) were sent to the vapor-liquid separator, where low vapor pressure species (GVL and PEA) were condensed, diluted in 5 mL of purified water (Type I) and quantified using a GC-FID detector (GC 7890A, Agilent) equipped with an Innowax column. To increase the solubility of PEA isomers in water (<2%) and thus prevent the formation of emulsions, reactor effluent streams with high concentrations of PEA (when *trans*-2-pentenoic acid was the reactant feed) were diluted in 5 mL of acetone/water (20% w/v) solution. High vapor pressure species, predominantly butene isomers and CO₂, were retained in the vapor phase and sent to the in-line GC (GC 7890A, Agilent) equipped with separate injectors, columns and detectors for hydrocarbons and CO₂. Butenes were resolved from residual oxygenates using an Innowax column and quantified using a calibrated FID response. CO₂ was resolved using an HP-PLOT/Q column and quantified using a calibrated TCD response relative to a helium reference.

Reaction conditions (catalyst loading, space time, temperature, and reactant partial pressure) were selected such that reactors operated differentially (<10% combined product

conversion), carbon balances closed to within 5%, and all targeted products were quantifiable. To that effect, it is assumed that reactant partial pressures differentials are insignificant along the catalyst bed and, bulk product partial pressures and surface coverages remain sufficiently low that they do not influence ring opening, ring closure and decarboxylation rates. To capture the interconversion between GVL and PEA isomers, reactant feeds comprised of GVL and *trans*-2-pentenoic acid in isolation rather than mixtures of the both. As reactors were operated differentially, observed reactant feed conversions (X_{GVL} and X_{PEA}) were mostly under 5%, and within precision range for GC analysis; therefore, reactant feed conversions were determined based on the formation of products as shown by Equations 7 and 8, where F_{C_4} , F_{PEA} , and F_{GVL} represent molar quantities of butene isomers, PEA isomers, and GVL in the reactor effluent, while F_{GVL0} and F_{PEA0} represent total molar quantities of GVL and *trans*-2-pentenoic acid fed into the reactor.

$$X_{GVL} = \frac{F_{C_4} + F_{PEA}}{F_{GVL0}} \quad \text{Equation 7}$$

$$X_{PEA} = \frac{F_{C_4} + F_{GVL}}{F_{PEA0}} \quad \text{Equation 8}$$

The interconversion between GVL and PEA was quantified by the observed extensive production rates of PEA isomers (with GVL used as reactant feed) or GVL (with *trans*-2-pentenoic acid used as reactant feed), and extensive production rates of butenes were quantified as decarboxylation rates. To obtain intensive rates of ring opening (ROR), ring closure (RCR), and decarboxylation (DC), observed extensive production rates of PEA isomers, GVL, and butene isomers, respectively, were normalized by the corresponding mass of catalyst loading as

shown by Equations 9, 10 and 11; where m_{cat} represents mass of catalyst loading, and R_{PEA} , R_{GVL} and R_{C_4} represent observed extensive production rates of PEA, GVL and butenes, respectively, in the reactor effluent determined by GC analysis. In addition, turn over frequencies (TOF) reported herein were obtained by dividing the corresponding mass-normalized rates by the molar density of Bronsted sites for the respective catalyst.

$$r_{ROR} = \frac{R_{PEA}}{m_{cat}} \quad \text{Equation 9}$$

$$r_{RCR} = \frac{R_{GVL}}{m_{cat}} \quad \text{Equation 10}$$

$$r_{DC} = \frac{R_{C_4}}{m_{cat}} \quad \text{Equation 11}$$

To probe the extent of catalyst deactivation and to avoid catalyst deactivation from masking reaction trends, reaction conditions were varied randomly and each experimental data set was collected using a “bracketing technique”. Typically, experimental data were first collected at a reference reaction condition; data were then collected by randomly varying a specific parameter (e.g., space time or reactant feed partial pressure); to complete the data set, data were again obtained at the reference condition. By employing the “bracketing technique” for each experimental data set, the difference in catalytic activity between the start and finish reference condition was determined. When the difference in catalytic activity was less than 5%, contributions from catalyst deactivation to the observed kinetics were deemed insignificant. However, experimental data set obtained within the same deactivation regime (linear deactivation profile), with a difference in catalytic activity greater than 5% (typically, $5\% \leq$

catalytic activity $\leq 20\%$), was adjusted for catalytic deactivation by assuming an exponential decay in the number of active sites over the course of the experiment, as shown by Equation 12, where r_x is the observed intensive mass-normalized rate (where $x = \text{DC}$, RCR or ROR), S_0 is the total number of active site on a given catalyst in pristine condition at start of experiment, k_d is the decay constant (determined from the slope of the plot of $\ln r_x$ versus t , employing reference condition data only), and t is the time.

$$r_x = S_0 e^{-k_d t} \quad \text{Equation 12}$$

3.3 Development of microkinetic model

The micokinetic model was developed from observations of studies designed to highlight the effects of space time, temperature, and reactant partial pressure. Experimental data were linearized using Arrhenius plots to determine apparent activation energies and pre-exponential factors, while Van't Hoff plots were used to determine apparent enthalpy- and entropy of reactions. Estimation of slopes was done using linear least squares and confidence intervals were evaluated at 95% confidence. Nonlinear least squares regressions to determine apparent forward rate constants and equilibrium constants were achieved on Microsoft Excel using the Solver function. MATLAB was used for robust nonlinear least squares regressions and to simultaneously solve sets of ordinary differential equations. The microkinetic model was calibrated using Campbell's degree of rate control,⁵⁸ and sensitivity of parameters was determined by measuring the change in predicted rates for a 1% perturbation in initial parameter values.

CHAPTER IV

RESULTS AND DISCUSSION

4.1 Catalyst activity versus time on stream

Recently, decarboxylation of GVL over $\text{SiO}_2/\text{Al}_2\text{O}_3$ to form butenes and CO_2 has been reported by Bond et al.⁵²⁻⁵³ At high temperatures (498–648 K), the authors reported two different regimes of catalyst deactivation: a rapid deactivation within the first 24 hours, associated with about 50% loss of initial activity, and a much slower rate of deactivation, with activity decreasing by about 0.4–0.5% per hour. In the same report,⁵² by employing temperature programmed oxidation studies on spent $\text{SiO}_2/\text{Al}_2\text{O}_3$, where predominantly CO and CO_2 products were observed (no butene oligomerization products); the initial activity of the spent $\text{SiO}_2/\text{Al}_2\text{O}_3$ catalyst was restored, and it was further established that the mode of deactivation was by the coke formation, probably from the polymerization of either GVL or PEA. From the above observations, deactivation of $\text{SiO}_2/\text{Al}_2\text{O}_3$ during GVL decarboxylation is reversible, allowing for periodic regeneration between experimental data sets.

To circumvent the rapid deactivation associated with $\text{SiO}_2/\text{Al}_2\text{O}_3$, reaction conditions (reaction temperature, pressure, and space time) were selected such that contribution from catalyst deactivation towards observed kinetic effects was insignificant (< 5%). For instance, Figures 10 and 11 show plots of mass-normalized extensive production rates of PEA isomers and butenes as functions of time on stream, respectively. In both figures, respective mass-normalized extensive production rates gradually increase as a function of time on stream until a steady-state production rate is reached, beyond which there is insignificant change in observed production

rates for extended time on stream (40 hours), implying that there is no meaningful loss in catalytic activity to impact observed kinetic effect.

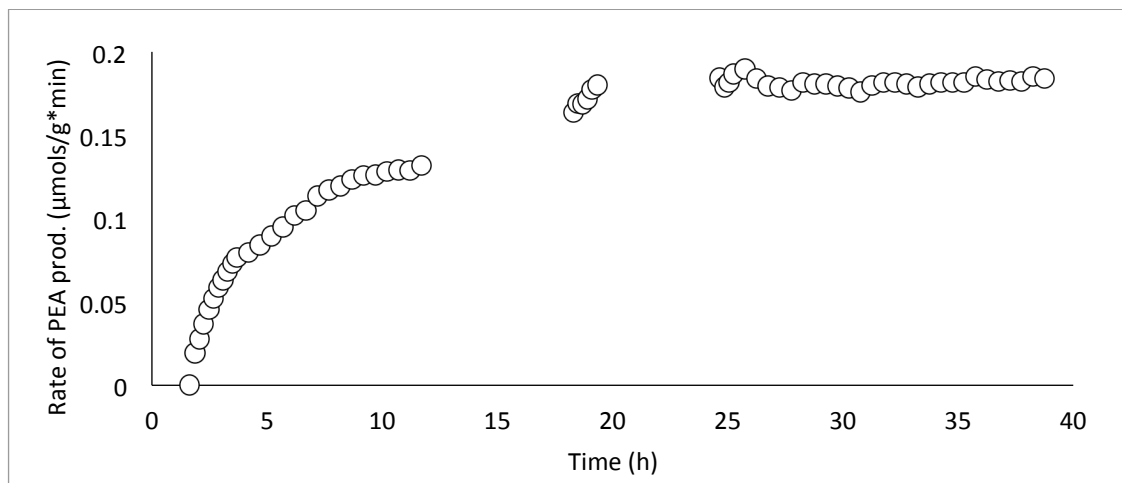


Figure 10. Mass-normalized production rates of PEA isomers as a function of time on stream; 2.8 mbar partial pressure of GVL; $T = 443.15\text{ K}$, space time (τ) = 15.75 min, 1.0 bar, and 1004 mg $\text{SiO}_2/\text{Al}_2\text{O}_3$.

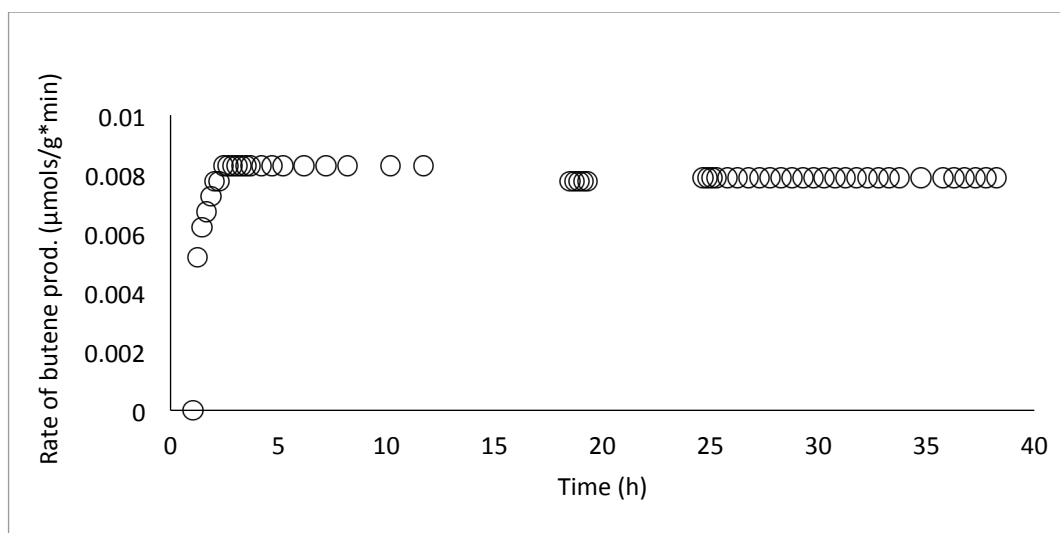


Figure 11. Mass-normalized production rates of butenes as a function of time on stream; 2.8 mbar partial pressure of GVL; $T = 443.15\text{ K}$, space time (τ) = 15.75 min, 1.0 bar, and 1004 mg $\text{SiO}_2/\text{Al}_2\text{O}_3$.

The observed trends showed a dependence on the total number of accessible Bronsted sites in the reactor, taking longer with increase in the total number of sites. In addition, for identical reaction conditions, increase in the partial pressure of the reactant lessened the duration of the transient to steady state production rates, implying that the transient is probably a surface adsorption transient. The transients associated with the extensive production rates of PEA isomers generally tended to take longer relative to those for the production rates of butene, indicating that the rate of exchange of adsorbed and gas-phase GVL is very rapid compared to the steady-state production rate of PEA isomers at the start of the experiment, until steady state production is reached when both processes are equilibrated. As noted in a previous study by Bond et al,⁵³ it appears that butene does not interact strongly with the catalyst surface so that its surface coverage remains considerably low making steady-state decarboxylation independent of the surface coverage of GVL and PEA.

4.2. Interconversion between GVL and PEA isomers

4.2.1 Partial pressure dependence

The dependence of mass-normalized rates of ring opening and decarboxylation on partial pressure of GVL is represented on Figure 12, from which apparent reaction orders of 0.025 ± 0.01 and 0.082 ± 0.01 were deduced for GVL ring opening and decarboxylation, respectively. Evidently, ring opening and decarboxylation both portray zero order dependence on GVL partial pressure. Thus, doubling GVL partial pressure has little or no effect on rates of both ring opening and decarboxylation, indicative of a strong interaction between GVL and the surface of $\text{SiO}_2/\text{Al}_2\text{O}_3$, which leads to saturation of accessible Bronsted acid sites and a neutral response to increased GVL partial pressure. In addition, the observation that ring opening and

decarboxylation follow the same reaction order with respect to GVL suggests that a single site reaction is involved in the formation of PEA isomers and butenes, involving an identical or structurally similar kinetically critical transition state and intermediate. This means that respectively stabilizing the transition state or destabilizing the intermediate could enhance the overall rate of reaction. This does not exclude the possibility of formation of butenes from intermediate PEA isomers; rather it implies that starting from either GVL or PEA, decarboxylation proceeds through a common transition state or intermediate.

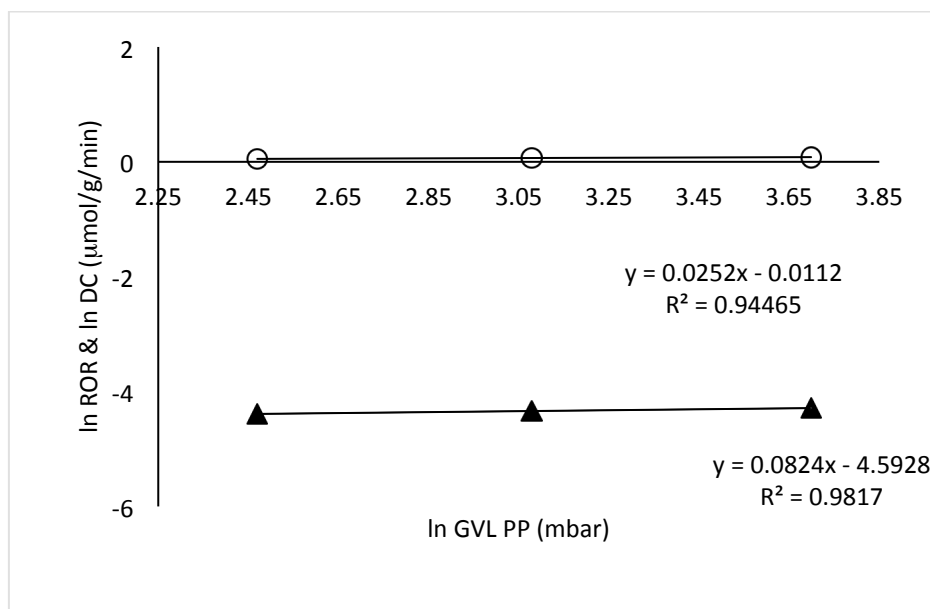


Figure 12. Dependence of ring opening and decarboxylation on partial pressure of GVL; T = 441.15 K, $\tau = 3.94$ min, 1 bar.

4.2.2. Determination of equilibrium conversion

As noted in Chapter 2, the formation of PEA isomers from GVL is reversible and attains equilibrium rapidly, unlike the decarboxylation step that is irreversible.⁵⁹ To effectively capture relevant kinetic and thermodynamic parameters of GVL ring opening and subsequent decarboxylation step; computational thermodynamic calculations were performed for the ring

opening step at 471 K, with the equilibrium conversion of GVL to PEA isomers determined to be about 5%, implying that the equilibrium is strongly favored toward GVL. To confirm, the equilibrium conversion of GVL to PEA was measured experimentally, using $\text{SiO}_2/\text{Al}_2\text{O}_3$ catalyst, at 471 K and ambient pressure, while holding GVL partial pressure fixed (10 mbar) and varying space time (0 – 35 min). As shown on Figure 13, conversion of GVL to PEA isomers increases gradually from zero, at zero space time, until it reaches equilibrium conversion of 5.1%, and remains constant with increasing space time. At shorter space times (0-2 min), conversion of GVL to PEA is kinetically controlled as conversion varies linearly with space time, while at longer space times (7-35 min), it is equilibrium-controlled, as conversion remains fixed. Over a range of short to long space times, the outlet concentrations of PEA and GVL vary, and the ratio becomes constant at longer space times when ring opening is equilibrium-controlled. This implies that the interconversion between GVL and PEA is equilibrated and for respective GVL partial pressures and temperatures, the ratio of outlet concentrations of PEA to GVL remains almost constant.

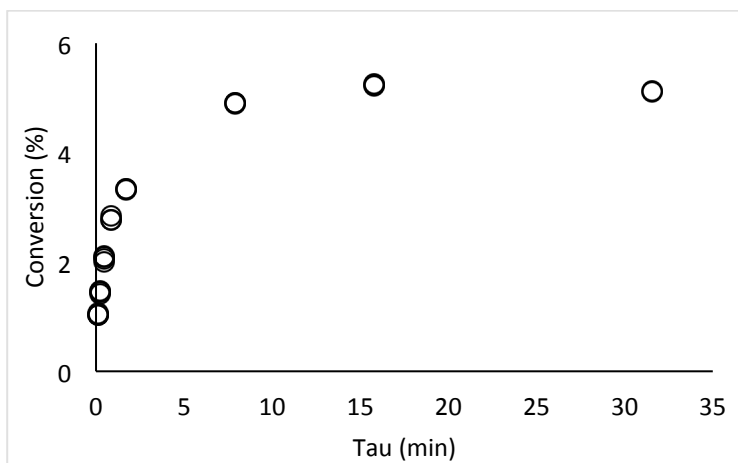


Figure 13. Determination of equilibrium conversion of GVL to PEA isomers on $\text{SiO}_2/\text{Al}_2\text{O}_3$, at 471 K, 1 bar, 10 mbar of GVL partial pressure.

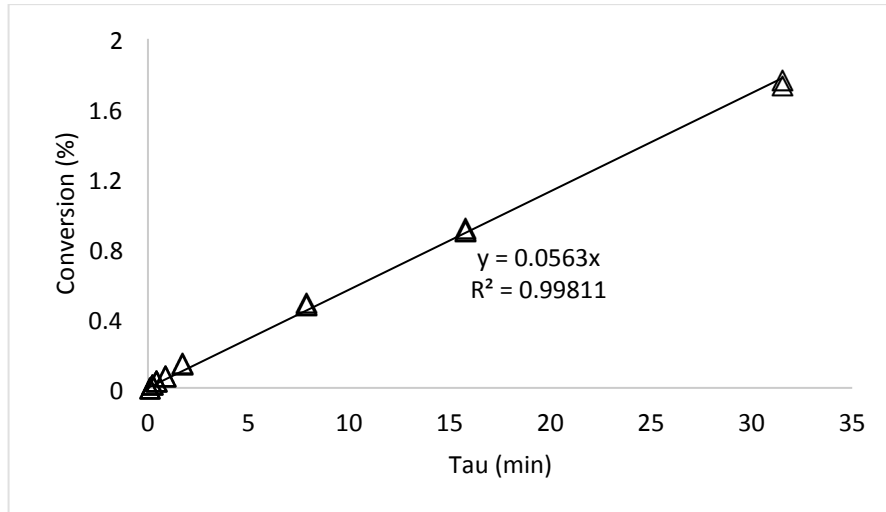


Figure 14. Conversion of GVL to butene isomers on $\text{SiO}_2/\text{Al}_2\text{O}_3$, at 471 K, 1 bar, and 10 mbar of GVL partial pressure.

On the contrary, spanning shorter to longer space times, the decarboxylation step is kinetically controlled (Figure 14), and the slope of the resultant profile corresponds to the apparent rate of decarboxylation and, given that decarboxylation is zero order with respect to GVL partial pressure, the apparent rate is equal to the forward rate constant.

4.2.3. Determination of kinetic and thermodynamic parameters

Figure 15 shows the ratio of measured outlet concentration of PEA to GVL as a function of space time. As mentioned earlier, over a range of shorter to longer space times, outlet concentrations of PEA and GVL vary and the ratio remains constant at longer contact times as equilibrium conversion is attained. Analogous to the conversion of GVL to PEA, measured outlet concentration ratios of PEA to GVL are kinetically controlled at shorter space times, and attain a constant ratio, when equilibrium conversion is reached at longer space times, where the reaction is equilibrium controlled.

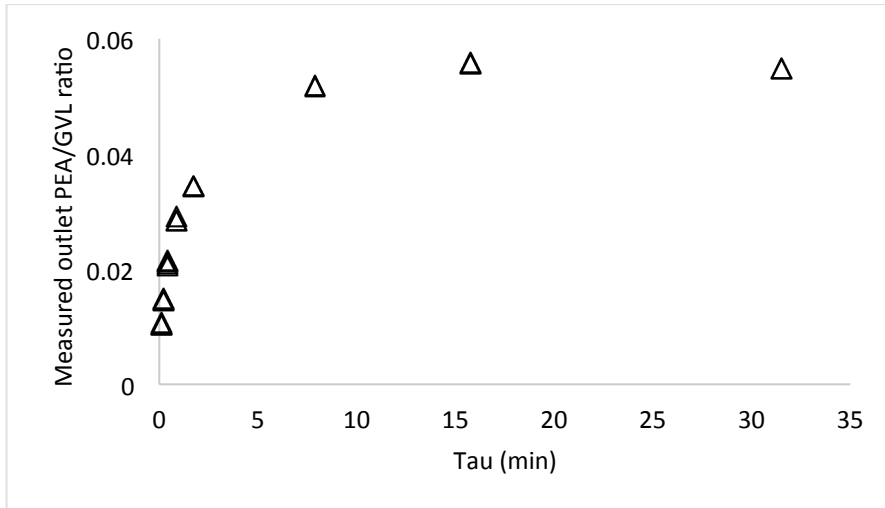


Figure 15. Measured outlet PEA to GVL ratio on $\text{SiO}_2/\text{Al}_2\text{O}_3$, at 471 K, 1 bar, 10 mbar of GVL partial pressure.

Ideally, the ring-opening step must be kinetically controlled over a range of shorter to longer space times for an apparent activation barrier and pre-exponential factor to be determined. However, because the equilibrium between GVL and PEA isomers is heavily favored toward GVL; at all GVL partial pressures and temperatures, the ring opening step rapidly attains equilibrium making it impossible for the ring opening step to be kinetically controlled over a wide range of space times. Principally, at very short space times where the ratio of measured outlet concentrations of PEA to GVL scales linearly with space time, GVL ring opening is far from equilibrated, and if the plot is extrapolated to zero space time, the slope gives a fair approximation of the apparent forward rate constant. Similarly, the horizontal region of the plot where the ratio of measured outlet concentrations of PEA to GVL is fixed, if extrapolated to ordinate axis affords an approximate value for the equilibrium constant.

Alternatively, apparent forward rate constants and equilibrium constants can be extracted from measured outlet concentrations of PEA/GVL ratios versus space time plots by fitting a model that captures the entire profile from shorter to longer space times. As experimental data

was obtained using a plug flow reactor (PFR); a model was derived by solving a gas-phase plug flow reactor in terms of extent of reaction and space time, as illustrated below. The derived model was used to fit experimental data, and through nonlinear regression optimization on Microsoft Excel (using Solver function); estimates for apparent forward rate constants and equilibrium constants were determined at different temperatures (Table 3).

Derivation of model

Step I: Derived mole balance for reversible equilibrium between GVL and PEA isomers in the gas phase, represented by $\text{GVL}_{(g)} \rightleftharpoons \text{PEA}_{(g)}$, and defined equilibrium constant, K , in terms of extent of reaction, ε , and GVL molar flow rate.

Table 2. Mole balance for reversible equilibrium between GVL and PEA isomers

Species	Inlet moles	Change in moles	Outlet moles
GVL	F_{GVLO}	$-\varepsilon$	$F_{GVLO} = F_{GVLO} - \varepsilon$
PEA	0	ε	$F_{PEA} = \varepsilon$
Total	F_{GVLO}	0	$F_{GVL} + F_{PEA} = F_{GVLO}$

The equilibrium constant, K , for the reversible reaction between GVL and PEA is defined in terms of activities as follows:

$$K = \frac{a_{PEA}}{a_{GVL}}$$

Where, $a_j = \frac{f_j}{f_j^o}$

f_j = Fugacity of species j

f_j^o = Fugacity of species j in standard state

Assuming an ideal gas mixture, the fugacity of each species is equal to its partial pressure, which in turn is a function of its equivalent mole fraction and total pressure, P_T , i.e.,

$$f_j = P_j = y_j P_T$$

And, the fugacity of the species in the standard state, $f_j^o = 1 \text{ atm}$ (because partial pressure of a pure component at 1 atm is 1 atm). Hence, the activities of the various species can be represented as:

$$a_j = \frac{P_j}{1 \text{ atm}}$$

Therefore, in terms of partial pressures, the equilibrium constant is defined as

$$K = \frac{P_{PEA}}{P_{GVL}}$$

Expressing P_{PEA} and P_{GVL} as a function of their equivalent mole fractions, system pressure and reference pressure, P^o ($P^o = 1 \text{ atm}$), using relations from the mole balance table,

$$P_{PEA} = \left(F_{PEA} / F_{GVLO} \right) \cdot \frac{P_T}{P^o}$$

And,

$$P_{GVL} = \left(F_{GVL} / F_{GVLO} \right) \cdot \frac{P_T}{P^o}$$

Expressing the equilibrium constant, K , in terms of extent of reaction, ε

$$K = \frac{\varepsilon}{F_{GVLO} - \varepsilon} = \frac{F_{PEA}}{F_{GVL}} \quad \text{Equation 13}$$

Thus far, from Equation 13, corroborates our initial analysis that at longer space times, the measured outlet concentration ratio of PEA/GVL is equal to the equilibrium constant at that respective temperature and GVL partial pressure.

Step II: Solved a gas-phase plug flow reactor in terms of extent of reaction, ε , and space time, τ , to derive a model from which apparent forward rate constants and equilibrium constants were estimated via non-linear regression optimization.

The material balance for a PFR is expressed as follows:

$$-\frac{dF_{GVL}}{dV} + r_{ROR} = \frac{dC_i}{dt}$$

The term on the right hand side (RHS) represents the accumulation term and vanishes to zero at steady state. The first term on the left hand side (LHS) is the convection term and the negative sign indicates that the initial concentration of GVL decreases axially across the length of the reactor. The second term on the LHS is the reaction term, representing how much GVL is consumed in the reaction and, for the reversible equilibrium between GVL and PEA, is defined as:

$$r_{ROR} = k_f \left(P_{GVL} - \frac{P_{PEA}}{K} \right)$$

Where k_f is the forward rate constant and the other terms carry the same representations as defined earlier.

At steady state, the PFR material balance reduces to

$$\frac{dF_{GVL}}{dV} = r_{ROR}$$

But,

$$V = \tau Q$$

Where V , τ and Q represent reactor volume, space time and volumetric flow rate, respectively.

From the mole balance table,

$$F_{GVL} = F_{GVLO} - \varepsilon$$

Substituting and solving the above referenced equations, the following equation is obtained.

$$\frac{K}{K + 1} \left[\ln \left(\frac{KF_{GVL} - F_{PEA}}{KF_{GVLO}} \right) \right] = \frac{Q\tau k_f}{F_{GVLO}} \quad \text{Equation 14}$$

Step III: Fitted model derived in *Step II* to experimental data to determine apparent forward rate constants and equilibrium constants.

Table 3 shows estimated apparent forward rate constants and equilibrium constants derived by fitting experimental data using nonlinear regression on Microsoft Excel (Solver function), to Equation 14.

Table 3. Estimated forward rate constants and equilibrium constants from PFR model.

T (K)	K	k (μmol/g/min)
441	0.0346	0.0018
451	0.0422	0.0040
471	0.0664	0.0157
491	0.0838	0.0623
509	0.1026	0.2477

The estimated apparent forward rate constants and equilibrium constants were linearized using Arrhenius and Van't Hoff plots, respectively. The apparent activation energy for GVL ring opening was estimated to be 133.12±12.22 kJ/mol and the pre-exponential factor to be 9.96×10¹² μmol/g/min (Figure 16). The enthalpy- and entropy of GVL ring opening were estimated at 30.22±6.89 kJ/mol and 40.83±14.63 kJ/mol, respectively (Figure 17).

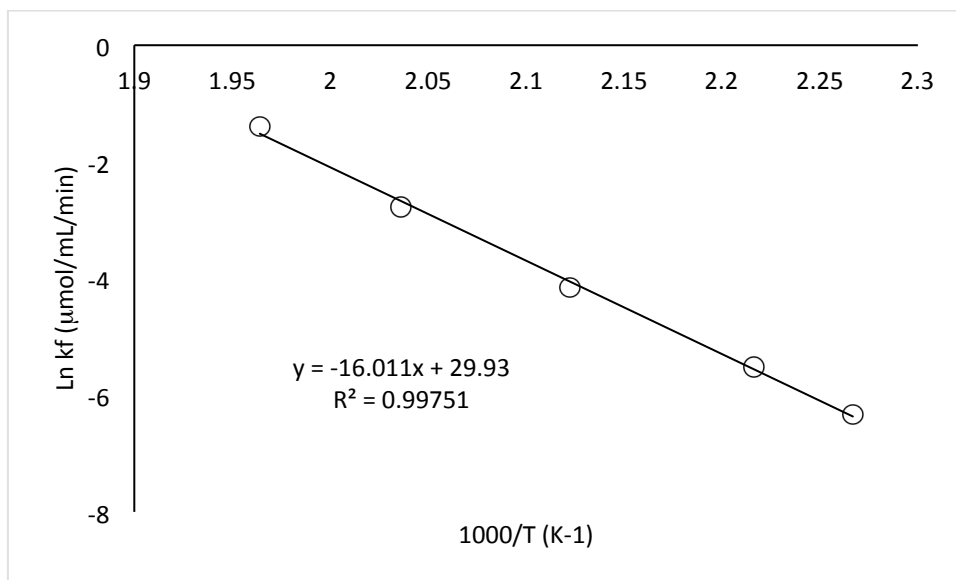


Figure 16. Estimated forward rate constants at different temperatures.

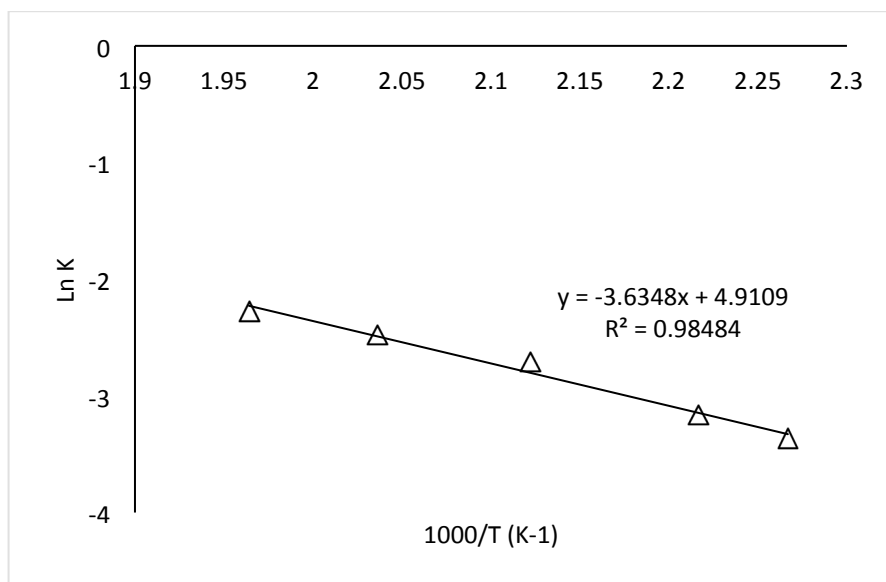


Figure 17. Estimated equilibrium constants at different temperatures.

The formation of PEA isomers through GVL ring opening is endothermic. In principle, the apparent activation energy for GVL ring opening should equal the sum of the enthalpy of ring opening and the apparent activation energy of PEA ring closure to form GVL (Figure 18). Having already determined the enthalpy of ring opening, measuring the apparent activation energy for PEA ring closure to GVL, would confirm the estimated apparent activation energy for GVL ring opening. In that respect, *trans*-2-pentenoic acid, which is the most stable PEA isomer, was used as reactant feed to determine the apparent activation energy for PEA ring-closure to GVL.

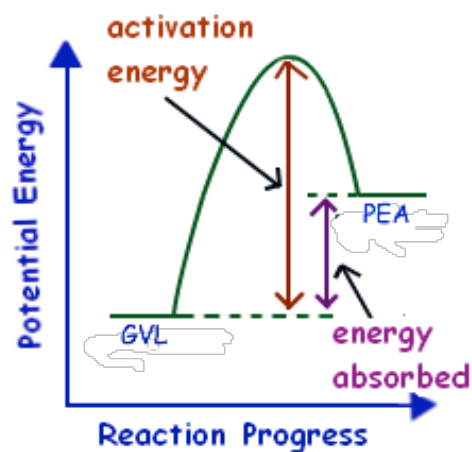


Figure 18. Relationship between activation energy and enthalpy of reaction during GVL to PEA interconversion.

As discussed earlier, the equilibrium between GVL and PEA isomers is thermodynamically favored toward GVL. Introducing PEA as the reactant feed will permit extensive production rates of GVL to be determined in a regime far enough from equilibrium, where ring closure of PEA to GVL is kinetically controlled. Unlike GVL ring opening to PEA, conversion of PEA to GVL scales linearly over a range of shorter to longer space times, confirming that measured ring closure rates are not influenced by the equilibrium between GVL and PEA isomers, and are kinetically controlled (Figure 19). The slope of the linear profile gives

the apparent reverse rate constant for ring closure of PEA to GVL, as the equilibrium between GVL and PEA also showed zero order dependence on PEA partial pressure.

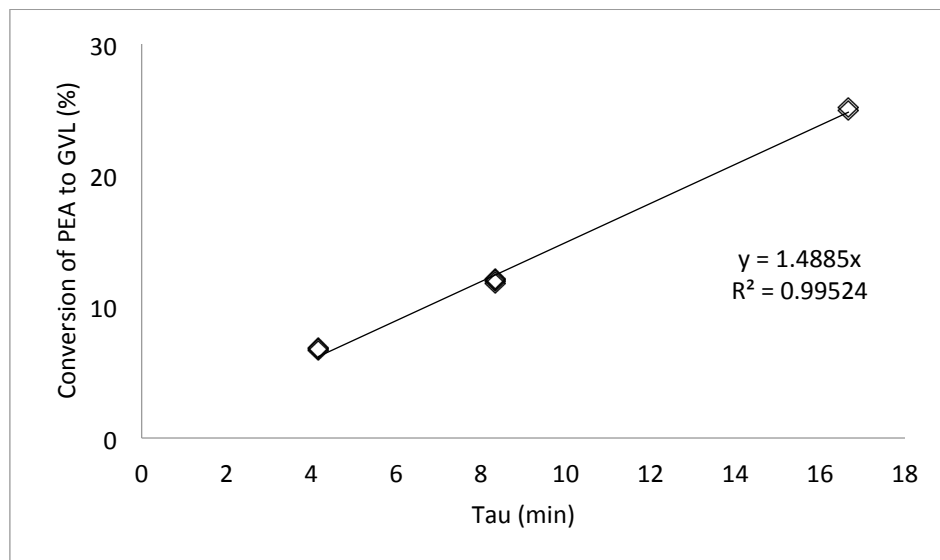


Figure 19. Conversion of PEA to GVL as a function of space time, 441 K, SiO₂/Al₂O₃, 10 mbar PEA partial pressure.

Table 4. Apparent reverse rate constants for PEA ring closure to GVL at various temperatures.

T (K)	k_r ($\mu\text{mol/g/min}$)
421	0.6894
431	1.4723
441	2.6288
451	5.1156
461	8.2777

Table 4 shows apparent reverse rate constant, (k_r) determined at different temperatures. Linearizing the obtained apparent reverse rate constants using an Arrhenius plot, the apparent activation energy for PEA ring closure and pre-exponential factor are determined to be 100.51 ± 9.08 kJ/mol and 2.11×10^{12} $\mu\text{mol/g/min}$, respectively (Figure 20). The estimated apparent activation energy for PEA ring closure when combined with the enthalpy of reaction is within

the range of the apparent activation energy for GVL ring opening, validating the estimated value of GVL ring opening to PEA derived from the PFR model (from Equation 14).

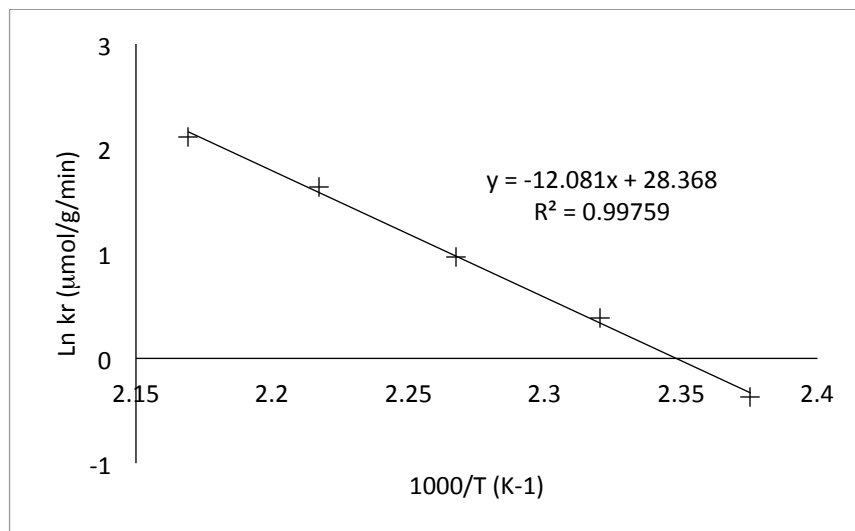


Figure 20. Apparent reverse rate constants of PEA ring closure to GVL as a function of temperature.

4.3 GVL and PEA decarboxylation

As presented earlier, decarboxylation of GVL over $\text{SiO}_2/\text{Al}_2\text{O}_3$, to produce butene isomers and CO_2 , shows zero order dependence on the partial pressure of GVL. While the ring opening step is thermodynamically unfavorable, the decarboxylation step is kinetically controlled and irreversible. With GVL ring opening, catalyst deactivation trends are masked by the equilibrium between GVL and PEA isomers, and are difficult to analyze. For decarboxylation, which is kinetically controlled, attendant deactivation trends become more conspicuous and as expected are more severe with increasing temperature.⁵⁹ At reaction temperatures where catalyst deactivation was rapid, typically showing pseudo-first order kinetics, deactivation constants were estimated from the slopes of plots of natural logarithm of

mass-normalized rates versus time on stream. By assuming an exponential decay in the initial number of active sites with time on stream, resultant deactivation constants were applied with Equation 12, to estimate theoretical decarboxylation rates at zero time on stream. Because catalyst deactivation was only observed at higher reaction temperatures, for consistency, the apparent activation energy and pre-exponential factor for decarboxylation were estimated from theoretical decarboxylation rates at zero time on stream, by linear regression.

Table 5. Theoretical decarboxylation rates at zero time on stream using PEA and GVL independently, as reactant feeds (10 mbar).

T (K)	PEA		GVL	
	k ($\mu\text{mol/g/min}$)	Confidence interval (95%)	k ($\mu\text{mol/g/min}$)	Confidence interval (95%)
451	0.0593	0.0007	-	-
471	0.3084	0.0074	0.1350	0.0015
491	1.0780	0.0203	0.6698	0.0137
509	2.8597	0.0622	1.6996	0.0431
519	5.2561	0.1983	3.1475	0.1293
538	-	-	9.5526	1.1785

Table 5 shows theoretical decarboxylation rates at zero time on stream obtained for decarboxylation of GVL and PEA over $\text{SiO}_2/\text{Al}_2\text{O}_3$ catalyst, respectively, at different temperatures. The apparent activation energies were estimated by linearizing the obtained theoretical decarboxylation rates on an Arrhenius plot (Figure 21). By introducing PEA as the reactant feed, an apparent activation energy of 126.28 ± 11.53 kJ/mol and pre-exponential factor of 2.77×10^{13} $\mu\text{mol/g/min}$ were estimated. With GVL as reactant feed, the apparent activation energy and pre-exponential factor were estimated to be 131.28 ± 13.89 kJ/mol and 5.48×10^{13} $\mu\text{mol/g/min}$, respectively.

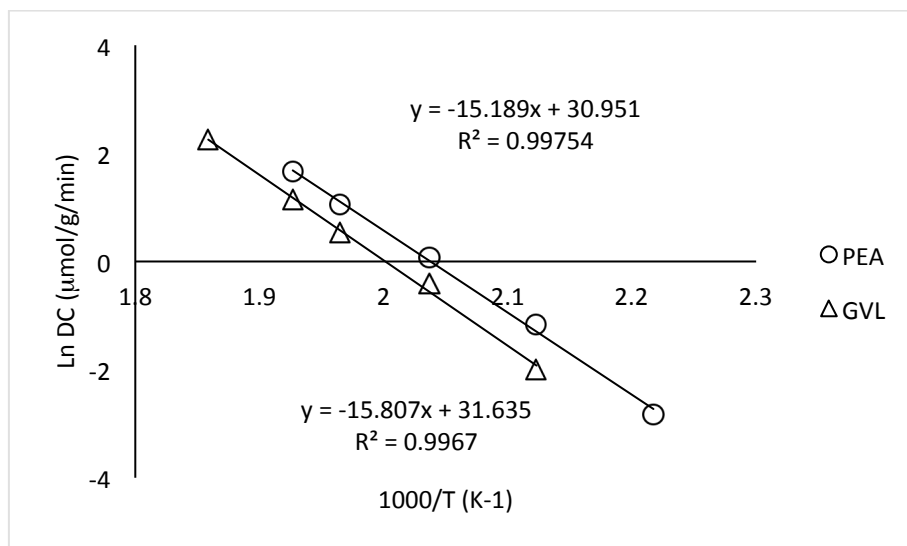


Figure 21. Decarboxylation rates of PEA and GVL introduced independently over $\text{SiO}_2/\text{Al}_2\text{O}_3$, at 10 mbar partial pressure, respectively and at different temperatures.

Apparently, switching the reactant feed from GVL to PEA doubles the pre-exponential factor (turn over frequency) but has insignificant effect on the apparent activation energy. This implies that decarboxylation of PEA and GVL over $\text{SiO}_2/\text{Al}_2\text{O}_3$ both proceeds through a common intermediate; however, the turn over frequency is faster when PEA is introduced as the reactant feed. In addition, these results further confirm that PEA is an intermediate in the decarboxylation of GVL over $\text{SiO}_2/\text{Al}_2\text{O}_3$, as previously reported by Bond et al.⁵⁹ Table 6 below summarizes the kinetic and thermodynamic parameters, determined experimentally, applied in the development of the microkinetic model.

Table 6. Summary of kinetic and thermodynamic parameters determined experimentally.

Parameter	Symbol	Description	Value
1	$E_{A,ROR}$	Activation barrier of GVL ring opening	133.12±12.22 kJ/mol
2	$A_{,ROR}$	Pre-exponential factor of GVL ring opening	9.96×10^{12} $\mu\text{mol/g/min}$
3	$E_{A,RCR}$	Activation barrier of PEA ring closure	100.51±9.08 kJ/mol
4	$A_{,RCR}$	Pre-exponential factor of PEA ring closure	2.11×10^{12} $\mu\text{mol/g/min}$
5	ΔH	Enthalpy of ring opening	30.22±6.89 kJ/mol
6	ΔS	Entropy of ring opening	40.83±14.63 kJ/mol K
7	$E_{A,DC,GVL}$	Activation barrier of GVL decarboxylation	131.28±13.89 kJ/mol
8	$A_{,DC,GVL}$	Pre-exponential factor of GVL decarboxylation	5.48×10^{13} $\mu\text{mol/g/min}$
9	$E_{A,DC,PEA}$	Activation barrier of PEA decarboxylation	126.28±11.53 kJ/mol
10	$A_{,DC,PEA}$	Pre-exponential factor of PEA decarboxylation	2.77×10^{13} $\mu\text{mol/g/min}$

4.4. Development of microkinetic model

In general, microkinetic analysis consolidates available experimental data, theoretical principles and appropriate relations fundamental to a catalytic process to form a unifying model, which elucidates key kinetic and/or thermodynamic parameters, reaction intermediates, surface coverages or mechanistic pathways governing the overall kinetics of the process. Unlike traditional kinetic models which start with initial assumptions designating a rate determining step or most abundant surface species; the development of a microkinetic model includes the kinetics of all elementary steps involved in the fundamental surface chemistry of the catalytic process,

with no arbitrary assumptions regarding mechanistic pathway, surface adsorbed species or rate-determining steps, and is not constrained to a particular set of conditions. Hence, a microkinetic model can be extrapolated to predict the behavior of catalytic processes involving similar reaction conditions, related reactants and products as well as similar catalytic materials. Such would be improbable with traditional kinetic models as initially assumed rate determining steps or surface coverages may be invalid outside the range of conditions.

4.4.1. Decarboxylation landscape

As presented in Chapter 2, decarboxylation of GVL over $\text{SiO}_2/\text{Al}_2\text{O}_3$ to form butene and CO_2 follows two mechanistic pathways (Figure 8).⁵⁹ As illustrated on Figure 22, the decarboxylation pathways presented on Figure 8 involve four classes of reaction. These reactions are (a) GVL ring opening to form C-4 carbenium ion (C-4 meaning positive charge is on the γ -carbon from the carboxylic acid group), (b) C-4 carbenium ion isomerizes to form PEA isomers, (c) C-4 carbenium ion undergoes a hydride shift to form C-3 carbenium ion, (d) C-3 carbenium ion decarboxylates to produce 1-butene and CO_2 .

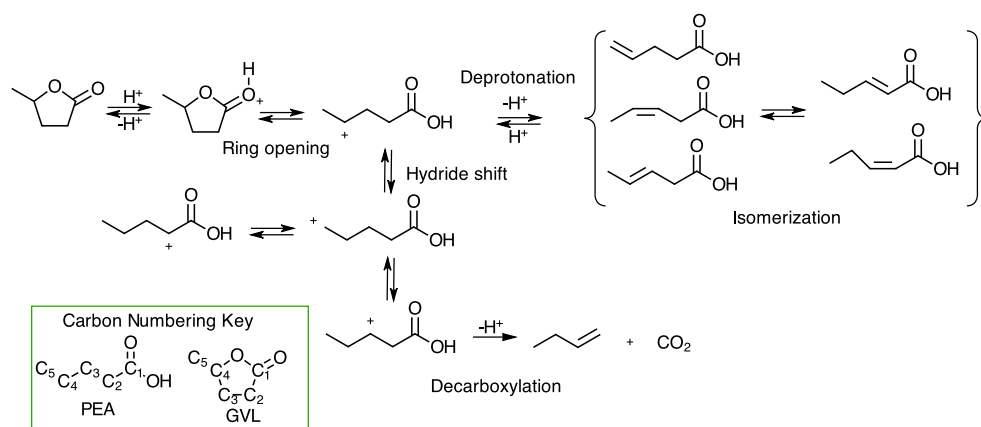
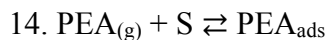


Figure 22. GVL reaction landscape over $\text{SiO}_2/\text{Al}_2\text{O}_3$

The GVL reaction landscape over SiO₂/Al₂O₃ can be expressed into 14 elementary reactions steps, involving nine surface adsorbed species, and three stable reaction products, as shown below. On the elementary reaction steps, S and B represent a vacant catalyst active and butene, respectively. X_{ads} represents a surface adsorbed species, where X identifies the species; and C-Y_{ads}, (where Y is a number), represents carbenium ions, with the number specifying the carbon atom possessing the positive charge of the carbenium ion. Summarily, reactions 1 and 2 represent GVL ring opening, reactions 3 through 5 represent hydride shifts, reactions 6 through 8, depict PEA isomerization, reaction 9 represents decarboxylation, while reaction 10 captures the isomerization of 1-butene to *cis*-2 butene and *trans*-2-butene, reactions 11 through 14 represent surface desorption steps.

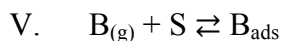
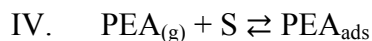
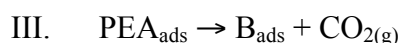
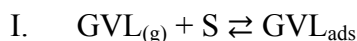
1. $\text{GVL}_{(g)} + \text{S} \rightleftharpoons \text{GVL}_{\text{ads}}$
2. $\text{GVL}_{\text{ads}} \rightleftharpoons \text{C-4}_{\text{ads}}$
3. $\text{C-4}_{\text{ads}} \rightleftharpoons \text{C-5}_{\text{ads}}$
4. $\text{C-5}_{\text{ads}} \rightleftharpoons \text{C-3}_{\text{ads}}$
5. $\text{C-3}_{\text{ads}} \rightleftharpoons \text{C-2}_{\text{ads}}$
6. $\text{C-3}_{\text{ads}} \rightleftharpoons \text{PEA}_{\text{ads}}$
7. $\text{C-4}_{\text{ads}} \rightleftharpoons \text{PEA}_{\text{ads}}$
8. $\text{C-2}_{\text{ads}} \rightleftharpoons \text{PEA}_{\text{ads}}$
9. $\text{C-3}_{\text{ads}} \rightleftharpoons \text{B}_{\text{ads}} + \text{CO}_{2(\text{ads})}$
10. $\text{B}_{\text{ads}} \rightleftharpoons \text{B}_{\text{ads}}$
11. $\text{B}_{(g)} + \text{S} \rightleftharpoons \text{B}_{\text{ads}}$
12. $\text{CO}_{2(g)} + \text{S} \rightleftharpoons \text{CO}_{2\text{ads}}$
13. $\text{GVL}_{(g)} + \text{S} \rightleftharpoons \text{GVL}_{\text{ads}}$



During experimental data analysis, equilibrium distributions of PEA isomers varied from shorter to longer space times, and in calculating outlet concentrations of PEA from GC chromatographs, combined areas of all detectable isomers were considered. To that effect, the apparent activation energy, pre-exponential factor, enthalpy of reaction and entropy of reaction for GVL ring opening to PEA isomers, determined earlier, are lumped parameters, encompassing reactions 2 through 8. According to Pearson acid base concept,⁶⁰ Bronsted sites on the surface of $\text{SiO}_2/\text{Al}_2\text{O}_3$ are hard centers and would interact strongly with carbenium ions, being hard acids. However, the equilibrium among carbenium ions, captured by reactions 2 through 5, is very rapid relative to ring opening and decarboxylation. At this time, we lack the resolution to quantify isomerization rates between carbenium ions; however, it is unlikely that they spend sufficient time on catalyst sites to influence surface coverages as well as the values of the lump constants determined experimentally. Consequently, in constructing the microkinetic model, reactions 2 through 8 were combined to form a single composite elementary reaction.

Analogous to the analysis of PEA isomers, equilibrium distributions of butene isomers varied from shorter to longer space times, so combined areas of butene isomers on GC chromatographs were used to determine outlet concentrations of butene. However, experimentally determined apparent activation energies and pre-exponential factors for production of butenes are representative for decarboxylation as the total amount of butenes produced were combined to get decarboxylation rates. To that respect, reaction 10 is embedded within reaction 9, and so will be excluded from further consideration for the construction of the microkinetic model.

Drawing from the discussions above, the initial 14 elementary reactions steps, without forfeiting any fundamental information relating to the mechanism, were reduced to 5 elementary reactions, consisting of 3 adsorbed species and 3 stable quantifiable products. These reactions were applied for the construction of the microkinetic model. The decarboxylation step, represented by Reaction III, is irreversible due to butenes and CO₂ being much lower in free energy than GVL and PEA. However, because carbon dioxide is a soft acid,⁶¹ upon production it would not readily bind to a Bronsted acid site, which is a hard center. Thus, the surface coverage of CO₂ at all times is significantly low and can be neglected.



The next step in constructing the microkinetic model was to estimate forward rate constants and equilibrium constants for all 5 elementary reactions, where applicable. This will provide insight as to which steps are fast enough to be assumed to be in equilibrium and which steps are slow enough to be considered rate-determining steps or simply neglected. In addition, familiarity with the forward rate constants and equilibrium constants for each elementary reaction will also provide insight about relative coverages of adsorbed species; allowing predictions to be made about which species are most abundant and which species are present in sufficiently low surface concentrations to be neglected.

The rates of the elementary reactions as well as the rates of change of surface coverage of adsorbed species with time are presented below; where k_f represents forward rate constant, θ_v represents vacant acid sites, θ_x represents surface coverage of species x , and P_x represents partial pressure of species x .

Rates of elementary reactions:

$$r_I = k_{fI} \left(P_{GVL} \theta_v - \frac{\theta_{GVL}}{K_I} \right)$$

$$r_{II} = k_{fII} \left(\theta_{GVL} - \frac{\theta_{PEA}}{K_{II}} \right)$$

$$r_{III} = k_{fIII} \theta_{PEA}$$

$$r_{IV} = k_{fIV} \left(P_{PEA} \theta_v - \frac{\theta_{PEA}}{K_{IV}} \right)$$

$$r_V = k_{fV} \left(P_B \theta_v - \frac{\theta_B}{K_V} \right)$$

Surface coverage of adsorbed species:

$$\frac{d\theta_{GVL}}{dt} = r_I - r_{II} = k_{fI} \left(P_{GVL} \theta_v - \frac{\theta_{GVL}}{K_I} \right) - k_{fII} \left(\theta_{GVL} - \frac{\theta_{PEA}}{K_{II}} \right)$$

$$\frac{d\theta_{PEA}}{dt} = r_{II} - r_{III} + r_{IV} = k_{fII} \left(\theta_{GVL} - \frac{\theta_{PEA}}{K_{II}} \right) - k_{fIII} \left(\theta_{PEA} - \frac{\theta_B P_{CO_2}}{K_{III}} \right) + k_{fIV} \left(P_{PEA} \theta_v - \frac{\theta_{PEA}}{K_{IV}} \right)$$

$$\frac{d\theta_B}{dt} = r_{III} - r_{IV} = k_{fIII} \left(\theta_{PEA} - \frac{\theta_B P_{CO_2}}{K_{III}} \right) - k_{fIV} \left(P_{PEA} \theta_v - \frac{\theta_{PEA}}{K_{IV}} \right)$$

$$\frac{d\theta_{CO_2}}{dt} = 0$$

$$\frac{d\theta_V}{dt} = -r_I - r_{IV} - r_V = -k_{fI} \left(P_{GVL} \theta_V - \frac{\theta_{GVL}}{K_I} \right) - k_{fIV} \left(P_{PEA} \theta_V - \frac{\theta_{PEA}}{K_{IV}} \right) - k_{fV} \left(P_B \theta_V - \frac{\theta_B}{K_V} \right)$$

4.4.2 Estimation of equilibrium constants

The equilibrium constant is defined as:

$$K = \exp(-\Delta G/RT)$$

where, ΔG is the Gibbs free energy, R is the universal gas constant, and T is the absolute temperature. The Gibbs free energy is a function of enthalpy, entropy and temperature and is defined as:

$$\Delta G = \Delta H - T\Delta S$$

where, ΔH is enthalpy, ΔS is entropy and T is absolute temperature. Hence, estimating Gibbs free energy for each elementary reaction entails knowing the corresponding enthalpies and entropies of all surface adsorbed species involved in the respective elementary reactions. The enthalpies of surface adsorbed species were deduced by subtracting the binding energy of the species to the catalyst surface from its corresponding gas phase enthalpy of reaction, at reaction temperature. Similarly, local entropies on the surface of the catalyst were estimated as one half of the difference between translational entropy and total entropy, in the gas phase, at reaction temperature. The translational entropies were estimated using the Sackur-Tetrode equation (Equation 15),^{58a} where S is the translational entropy, R is the universal gas constant, T is the absolute temperature, P is pressure, k_B is Boltzmann constant, h is Planck's constant, m is the molecular weight of species, and N is Avogadro's number.

$$S = R \ln \frac{(2\pi m k_B T)^{3/2} k_B T}{h^3 N^{5/2} P} + \frac{5}{2} R \quad \text{Equation 15}$$

When the gas phase species bind to the catalyst surface, there is a change in translational entropy. In principle, the species in the gas phase and the acid site each have three degrees of translational freedom; upon adsorption, the resultant surface species has a total of three degrees of translational freedom and the remaining three degrees of freedom reflect vibrations of the species while on the acid site. Although the vibrational entropy can be calculated from Equation 16, difficulties associated with guessing a reasonable value of ν , for assumed vibrational modes, erroneously influences the outcome of the calculation. Thus local entropies are approximated as one half of the difference between the gas phase translational entropies and total entropies, to account for the vibrational entropy.⁶³

$$S_{vibr} = N k_b \left(\frac{h\nu/k_B T}{e^{h\nu/k_b T}} - \ln \left(1 - e^{-h\nu/k_b T} \right) \right) \quad \text{Equation 16}$$

where k_B is the Boltzmann constant, h is the Planck's constant, T is absolute temperature, ν is the frequency of the vibrational mode, and N is the Avogadro's number.

4.4.3 Estimation of forward rate constants

The forward rate constants for the elementary reaction steps were evaluated from an Arrhenius expression:

$$k_f = A \exp \left(-E_A / RT \right)$$

where k_f is the forward rate constant, A is the pre-exponential factor, E_A is the apparent activation energy, R is the gas constant, and T is the absolute temperature. Following Waugh et

al,⁶² the pre-exponential factors for surface reactions as well as adsorption and desorption process were assumed to be 10^{13} s^{-1} . Although activation energies for the forward rate constants can be estimated from heats of reaction, using the Polanyi expression:⁶³

$$E_A = E_0 + \alpha H \text{ for exothermic reactions}$$

$$E_A = E_0 + (1 - \alpha)H \text{ for endothermic reactions}$$

where H is the heat of reaction, α is position of the transition state along the reaction coordinate and has limits $0 \leq \alpha \leq 1$, and E_0 is the activation energy of a reference reaction; experimentally determined activation energies for GVL ring opening and decarboxylation were used. Because GVL, PEA and butene stick to the surface of $\text{SiO}_2/\text{Al}_2\text{O}_3$, making the sticking coefficient, even at low coverages, to be close to unity, surface adsorption and desorption elementary steps are assumed to be unactivated, so the temperature coefficients of the rates of adsorption are significantly small and the corresponding activation energies are negligible.

With estimates for the forward rate constants and equilibrium constants, the surface coverage equations presented earlier, alongside the surface sites balance equation, were solved simultaneously using a transient CSTR to obtain steady state surface coverage for all surface adsorbed species.

4.4.4 Microkinetic model calibration

Having developed the microkinetic model, Campbell's degree of rate control was used to assess the sensitivity of the rate constants estimated for all the elementary reaction steps involved.⁵⁸ In general, Campbell's degree of rate control (Equation 17) assesses the extent to which a differential change in the forward and reverse rate constants for each step affects the fractional increase in the overall rate of reaction. Typically, the differential change is 1% so that

the equilibrium constant remains fixed. The step that leads to the greatest fractional increase in overall rate is the most rate-controlling. The degree to which a step controls the overall rate is the percent increase in the overall rate normalized by 1%. For all elementary steps, the sum of the respective degrees of rate control is equal to unity (Equation 18).

$$X_{RC,i} = \frac{k_i}{r} \left(\frac{\partial r}{\partial k_i} \right)_{k_{j \neq i}, K_i} = \left(\frac{\partial \ln r}{\partial \ln k_i} \right)_{k_{j \neq i}, K_i} \quad \text{Equation 17}$$

$$\sum_i X_{RC,i} = 1 \quad \text{Equation 18}$$

Where $X_{RC,i}$ is the degree of rate control, r is the rate of reaction, k_j represents rate constant for step j ($j \neq i$) and K_i represents equilibrium constant for step i .

From our sensitivity studies applying Campbell's degree of rate control,^{58b} shown on Table 7, two sensitive parameters were identified: the apparent forward rate constant for GVL ring opening and the free energy of adsorption of GVL to the catalyst surface.

Table 7. Degree of rate control for key elementary steps.

Elementary step	Description	$X_{RC,i}$ (1%) -- DC	$X_{RC,i}$ (1%) -- ROR
I	GVL adsorption	0	0
II	PEA adsorption	0	0
III	Butene adsorption	0	0
IV	Ring opening	0	0.9750
V	Decarboxylation	1.0463	0

Analogously, Campbell's degree of thermodynamic control (Equation 19) was used to determine the sensitivity of surface intermediates. In principle, this assesses the extent to which the stability of an intermediate on the surface of the catalyst affects the overall rate of reaction. This is achieved by changing (~ 1% perturbation) the standard free energy of a species without changing anything else and determining how that influences the fractional increase in overall reaction rate.

$$X_{TRC,n} = \frac{1}{r} \left(\frac{\partial r}{\partial \left(\frac{-G_n^0}{RT} \right)} \right)_{G_m^0, G_i^{0,TS}} = \left(\frac{\partial \ln r}{\partial \left(\frac{-G_n^0}{RT} \right)} \right)_{G_m^0, G_i^{0,TS}} \quad \text{Equation 19}$$

Where $X_{TRC,n}$ is the degree of thermodynamic rate control, n represents an intermediate, R is the gas constant, T is the absolute temperature, and $G_i^{0,TS}$ is the Gibbs free energy of transition state i , G_n^0 Gibbs free energy for intermediate n , and $m \neq n$. $X_{TRC,n}$ is dimensionless and specific reference conditions must be defined for each standard state. From Table 8, a 1 % perturbation in the binding energies of GVL, butenes, and PEA to the catalyst surface show that the adsorption of GVL is important for ring opening while that of PEA is significant for decarboxylation.

Table 8. Degree of thermodynamic rate control for key intermediates.

Species	Binding Energy (kJ/mol)	$X_{TRC,n}$ (1%) -- DC	$X_{TRC,n}$ (1%) -- ROR
GVL _{ads}	50	0	-0.0046
PEA _{ads}	50	-0.0059	0
B _{ads}	50	0	0

Based on the microkinetic analysis, GVL ring opening to PEA was identified as a rate-controlling step. This is indicative that the ring opening step to form the carbenium ion with the charge on the γ -carbon from the carboxylic acid group is probably the rate determining step in the reaction mechanism, implying that destabilizing the aforementioned carbenium ion should increase the overall rate of GVL decarboxylation. Further, for subsequent experimental measurements, it would be of interest to accurately measure the apparent forward rate constant, as it is kinetically relevant to GVL decarboxylation. These predictions also offer a potential explanation to the observation by Kellicutt et al⁵⁵ that Bronsted sites on ASA and MFI zeolites; with comparable deprotonation energies and apparent activation barriers to GVL decarboxylation had markedly different TOFs. In their study, Kellicutt et al reported on deprotonation energies and apparent activation barriers to decarboxylation, without consideration of the kinetics of the ring opening step. Although the deprotonation energy is indicative of the relative ease with which GVL can bind to the surface, and subsequently ring open; it offers no information about the kinetics of the ring opening step. The prediction from the microkinetic analysis that adsorption of GVL to the catalyst surface and subsequent ring opening are kinetically relevant, suggests that the difference in TOFs reported by Kellicutt et al is probably an artifact of local structural effects of the Bronsted sites. The adsorption of GVL on a Bronsted site is unactivated; therefore, if deprotonation energies are comparable, it implies that the relative ease to ring opening should be comparable, as well as subsequent decarboxylation, unless influenced by the structure of the Bronsted site.

CHAPTER V CONCLUSION AND FUTURE DIRECTION

5.1 Conclusion

In this project, we have shown that a reliable microkinetic model for GVL decarboxylation to butene and CO₂ over SiO₂/Al₂O₃ may be developed from a simplistic evaluation of the rate constants, apparent activation barriers and energetics of the elementary reaction steps involved in the mechanism. The model quantitatively describes the kinetics of GVL decarboxylation over SiO₂/Al₂O₃, identifying the adsorption of GVL to the catalyst surface and subsequent ring opening step as two steps that dominate the kinetics of the process.

The microkinetic model predicts the surface adsorption and ring opening steps as kinetically relevant elementary steps, in the future, it would be important to further probe experimentally the relative importance of these steps, independently. To further investigate the surface adsorption step, a possible option would be to consider other aluminosilicate catalysts with different pore sizes. Of particular interest will be MFI zeolites, because they are microporous and have a pore diameter similar to the molecular diameter of GVL, meaning that GVL might have restricted access through the pore of the catalyst, which affects the rate of transfer of gas-phase GVL from the bulk stream to the surface of the catalyst. However, as the deprotonation energies of ASA and MFI zeolites are comparable, deprotonation and subsequent ring opening should be comparable. Similarly, to further probe the ring opening step, a potential catalyst would be PWA/SiO₂, which allows unrestricted access to the acid site, but possesses lower deprotonation energy relative to SiO₂/Al₂O₃, implying that the ring opening would be much faster. Another potential study would be to screen solid acid materials that can destabilize the carbenium ion formed from ring opening of GVL, which would increase the overall rate of decarboxylation. In a nutshell, these recommended studies would further elucidate our findings

that the surface adsorption and ring opening steps are kinetically relevant and such information would be beneficial as the search for a more active and stable catalyst for GVL decarboxylation moves forward.

REFERENCES

1. (a) BP energy outlook sees 41% rise in worldwide energy use to 2035. *Oil Gas J* **2014**, *112* (1c), 20–21; (b) IEA's World Energy Outlook 2013: Renewables and natural gas to Surge Through 2035. *Power* **2014**, *158* (1), 8–9; (c) Thinnes, B., Global energy outlook to 2035. *Hydrocarb Process* **2011**, *90* (1), 17–18.
2. H. D. R. http://hdr.undp.org/sites/default/files/hdr_2015_statistical_annex.pdf (accessed 01/04/2016).
3. U. S. Environmental Protection Agency <http://www3.epa.gov/climatechange/ghgemissions/gases.html> (accessed 01/04/16).
4. Hassol, S. J. Questions and answers: Emissions reductions needed to stabilize climate. <https://www.climatecommunication.org/wp-content/uploads/2011/08/presidentialaction.pdf>.
5. (a) Alonso, D. M.; Bond, J. Q.; Serrano-Ruiz, J. C.; Dumesic, J. A., Production of liquid hydrocarbon transportation fuels by oligomerization of biomass-derived C9 alkenes. *Green Chem.* **2010**, *12* (6), 992–999; (b) Azadi, P.; Inderwildi, O. R.; Farnood, R.; King, D. A., Liquid fuels, hydrogen and chemicals from lignin: A critical review. *Renewable Sustainable Energy Rev.* **2013**, *21*, 506–523; (c) Bozell, J. J.; Moens, L.; Elliott, D. C.; Wang, Y.; Neuenschwander, G. G.; Fitzpatrick, S. W.; Bilski, R. J.; Jarnefeld, J. L., Production of levulinic acid and use as a platform chemical for derived products. *Resour Conserv Recy* **2000**, *28* (3–4), 227–239; (d) Braden, D. J.; Henao, C. A.; Heltzel, J.; Maravelias, C. C.; Dumesic, J. A., Production of liquid hydrocarbon fuels by catalytic conversion of biomass-derived levulinic acid. *Green Chem.* **2011**, *13* (7), 1755–1765.
6. (a) Cheng, S. M.; Zhu, S. D., Lignocellulosic Feedstock Biorefinery-the future of the chemical and energy industry. *Bioresources* **2009**, *4* (2), 456–457; (b) Alonso, D. M.; Bond, J. Q.; Dumesic, J. A., Catalytic conversion of biomass to biofuels. *Green Chem* **2010**, *12* (9), 1493–1513.
7. (a) Huber, G. W.; Corma, A., Synergies between bio- and oil refineries for the production of fuels from biomass. *Angew Chem Int Edit* **2007**, *46* (38), 7184–7201; (b) Chang, H. N.; Kim, N. J.; Kang, J.; Jeong, C. M., Biomass-derived volatile fatty acid platform for fuels and chemicals. *Biotechnol Bioproc E* **2010**, *15* (1), 1–10.
8. R. Davis, L. T., E.C.D. Tan, M.J. Bidy, G.T. Beckham, and C. Scarlata., Process design and economics for the conversion of lignocellulosic biomass to hydrocarbons:dilute-acid and enzymatic deconstruction of biomass to sugars and biological conversion of sugars to hydrocarbons; 2013.

9. Wyman, C. E.; Dale, B. E.; Elander, R. T.; Holtzaple, M.; Ladisch, M. R.; Lee, Y. Y., Coordinated development of leading biomass pretreatment technologies. *Bioresource Technol* **2005**, *96* (18), 1959–1966.
10. Wyman, C. E.; Dale, B. E.; Elander, R. T.; Holtzaple, M.; Ladisch, M. R.; Lee, Y. Y., Comparative sugar recovery data from laboratory scale application of leading pretreatment technologies to corn stover. *Bioresource Technol* **2005**, *96* (18), 2026–2032.
11. (a) Gallezot, P., Conversion of biomass to selected chemical products. *Chem Soc Rev* **2012**, *41* (4), 1538–1558; (b) Mamman, A. S.; Lee, J. M.; Kim, Y. C.; Hwang, I. T.; Park, N. J.; Hwang, Y. K.; Chang, J. S.; Hwang, J. S., Furfural: Hemicellulose/xyloso-derived biochemical. *Biofuel Bioprod Bior* **2008**, *2* (5), 438–454.
12. Zakzeski, J.; Bruijninx, P. C. A.; Jongerius, A. L.; Weckhuysen, B. M., The Catalytic valorization of lignin for the production of renewable chemicals. *Chem Rev* **2010**, *110* (6), 3552–3599.
13. Zakzeski, J.; Jongerius, A. L.; Weckhuysen, B. M., Transition metal catalyzed oxidation of Alcell lignin, soda lignin, and lignin model compounds in ionic liquids. *Green Chem* **2010**, *12* (7), 1225–1236.
14. (a) Agler, M. T.; Wrenn, B. A.; Zinder, S. H.; Angenent, L. T., Waste to bioproduct conversion with undefined mixed cultures: the carboxylate platform. *Trends Biotechnol* **2011**, *29* (2), 70–78; (b) Weimer, P. J.; Russell, J. B.; Muck, R. E., Lessons from the cow: What the ruminant animal can teach us about consolidated bioprocessing of cellulosic biomass. *Bioresource Technol* **2009**, *100* (21), 5323–5331.
15. Serrano-Ruiz, J. C.; Braden, D. J.; West, R. M.; Dumesic, J. A., Conversion of cellulose to hydrocarbon fuels by progressive removal of oxygen. *Appl. Catal., B* **2010**, *100* (1–2), 184–189.
16. Cai, C. M.; Zhang, T.; Kumar, R.; Wyman, C. E., Integrated furfural production as a renewable fuel and chemical platform from lignocellulosic biomass. *J. Chem. Technol. Biotechnol.* **2014**, *89* (1), 2–10.
17. (a) Liu, C. G.; Wyman, C. E., Partial flow of compressed-hot water through corn stover to enhance hemicellulose sugar recovery and enzymatic digestibility of cellulose. *Bioresource Technol* **2005**, *96* (18), 1978–1985; (b) Lloyd, T. A.; Wyman, C. E., Combined sugar yields for dilute sulfuric acid pretreatment of corn stover followed by enzymatic hydrolysis of the remaining solids. *Bioresource Technol* **2005**, *96* (18), 1967–1977; (c) Hu, L.; Zhao, G.; Hao, W.; Tang, X.; Sun, Y.; Lin, L.; Liu, S., Catalytic conversion of biomass-derived carbohydrates into fuels and chemicals via furanic aldehydes. *RSC Adv.* **2012**, *2* (30), 11184–11206.
18. Elliott, D. C., Historical developments in hydroprocessing bio-oils. *Energ Fuel* **2007**, *21* (3), 1792–1815.

19. Zhao, Y.; Fu, Y.; Guo, Q.-X., Production of aromatic hydrocarbons through catalytic pyrolysis of γ -valerolactone from biomass. *Bioresour. Technol.* **2012**, *114*, 740–744.
20. Hoang, T. M. C.; Lefferts, L.; Seshan, K., Valorization of humin-based byproducts from biomass processing: a route to sustainable hydrogen. *Chemsuschem* **2013**, *6* (9), 1651–1658.
21. (a) Tang, X.; Chen, H.; Hu, L.; Hao, W.; Sun, Y.; Zeng, X.; Lin, L.; Liu, S., Conversion of biomass to γ -valerolactone by catalytic transfer hydrogenation of ethyl levulinate over metal hydroxides. *Appl. Catal., B* **2014**, *147*, 827–834; (b) Tukacs, J. M.; Kiraly, D.; Stradi, A.; Novodarszki, G.; Eke, Z.; Dibo, G.; Kegl, T.; Mika, L. T., Efficient catalytic hydrogenation of levulinic acid: a key step in biomass conversion. *Green Chem.* **2012**, *14* (7), 2057–2065; (c) Upare, P. P.; Lee, J.-M.; Hwang, D.-W.; Halligudi, S. B.; Hwang, Y.-K.; Chang, J.-S., Selective hydrogenation of levulinic acid to γ -valerolactone over carbon-supported noble metal catalysts. *J. Ind. Eng. Chem. (Amsterdam, Neth.)* **2011**, *17* (2), 287–292.
22. Holladay, J. D.; Hu, J.; King, D. L.; Wang, Y., An overview of hydrogen production technologies. *Catal Today* **2009**, *139* (4), 244–260.
23. (a) Hengne, A. M.; Kamble, S. B.; Rode, C. V., Single pot conversion of furfuryl alcohol to levulinic esters and γ -valerolactone in the presence of sulfonic acid functionalized ILs and metal catalysts. *Green Chem.* **2013**, *15* (9), 2540–2547; (b) Johnson, T. C.; Morris, D. J.; Wills, M., Hydrogen generation from formic acid and alcohols using homogeneous catalysts. *Chem Soc Rev* **2010**, *39* (1), 81–88.
24. Hall, R. L.; Oser, B. L., Recent Progress in Consideration of flavoring ingredients under food additives amendment .3. gras substances. *Food Technol-Chicago* **1965**, *19* (2p2), 151.
25. Horvath, I. T.; Mehdi, H.; Fabos, V.; Boda, L.; Mika, L. T., gamma-Valerolactone - a sustainable liquid for energy and carbon-based chemicals. *Green Chem* **2008**, *10* (2), 238–242.
26. Horvath, I. T., Solvents from nature. *Green Chem* **2008**, *10* (10), 1024–1028.
27. Lange, J. P.; Vestering, J. Z.; Haan, R. J., Towards 'bio-based' Nylon: conversion of gamma-valerolactone to methyl pentenoate under catalytic distillation conditions. *Chem Commun* **2007**, (33), 3488–3490.
28. (a) Lange, J.-P.; Price, R.; Ayoub, P. M.; Louis, J.; Petrus, L.; Clarke, L.; Gosselink, H., Valeric biofuels: A platform of cellulosic transportation fuels. *Angew. Chem., Int. Ed.* **2010**, *49* (26), 4479–4483, S4479/1-S4479/4; (b) Du, X.-L.; Bi, Q.-Y.; Liu, Y.-M.; Cao, Y.; He, H.-Y.; Fan, K.-N., Tunable copper-catalyzed chemoselective hydrogenolysis of biomass-derived γ -valerolactone into 1,4-pentanediol or 2-methyltetrahydrofuran. *Green Chem.* **2012**, *14* (4), 935–939.

29. Luisa, M.; Pilcher, G.; Yang, M. Y.; Brown, J. M.; Conn, A. D., Enthalpies of Combustion of gamma-butyrolactone, gamma-valerolactone, and delta-valerolactone. *J Chem Thermodyn* **1990**, *22* (9), 885–891.
30. (a) Fabos, V.; Mika, L. T.; Horvath, I. T., Selective Conversion of levulinic and formic acids to γ -valerolactone with the Shvo Catalyst. *Organometallics* **2014**, *33* (1), 181–187; (b) Kon, K.; Onodera, W.; Shimizu, K.-i., Selective hydrogenation of levulinic acid to valeric acid and valeric biofuels by a Pt/HMFI catalyst. *Catal. Sci. Technol.* **2014**, *4* (9), 3227–3234; (c) Li, M.; Li, G.; Li, N.; Wang, A.; Dong, W.; Wang, X.; Cong, Y., Aqueous phase hydrogenation of levulinic acid to 1,4-pentanediol. *Chem. Commun. (Cambridge, U. K.)* **2014**, *50* (12), 1414–1416.
31. (a) Deng, L.; Zhao, Y.; Li, J.; Fu, Y.; Liao, B.; Guo, Q.-X., Conversion of levulinic acid and formic acid into γ -valerolactone over heterogeneous catalysts. *Chemsuschem* **2010**, *3* (10), 1172–1175; (b) Du, X.; Liu, Y.; Wang, J.; Cao, Y.; Fan, K., Catalytic conversion of biomass-derived levulinic acid into γ -valerolactone using iridium nanoparticles supported on carbon nanotubes. *Cuihua Xuebao* **2013**, *34* (5), 993–1001.
32. Peng, L.; Lin, L.; Li, H., Extremely low sulfuric acid catalyst system for synthesis of methyl levulinate from glucose. *Ind. Crops Prod.* **2012**, *40*, 136–144.
33. (a) Fitzpatrick, S. W., Biofine process: A biorefinery concept based on thermochemical conversion of biomass. *Abstr Pap Am Chem S* **2004**, *227*, U306–U306; (b) Fitzpatrick, S. W., The Biofine technology A "bio-refinery" concept based on thermochemical conversion of cellulosic biomass. *Acs Sym Ser* **2006**, *921*, 271–287; (c) Fitzpatrick, S. W., Thermocatalytic biorefining of biomass via the Biofine process. *Abstr Pap Am Chem S* **2011**, *241*.
34. Villaverde, M. M.; Bertero, N. M.; Garetto, T. F.; Marchi, A. J., Selective liquid-phase hydrogenation of furfural to furfuryl alcohol over Cu-based catalysts. *Catal. Today* **2013**, *213*, 87–92.
35. Neves, P.; Lima, S.; Pillinger, M.; Rocha, S. M.; Rocha, J.; Valente, A. A., Conversion of furfuryl alcohol to ethyl levulinate using porous aluminosilicate acid catalysts. *Catal. Today* **2013**, *218–219*, 76–84.
36. (a) Tang, X.; Hu, L.; Sun, Y.; Zhao, G.; Hao, W.; Lin, L., Conversion of biomass-derived ethyl levulinate into γ -valerolactone via hydrogen transfer from supercritical ethanol over a ZrO₂ catalyst. *RSC Adv.* **2013**, *3* (26), 10277–10284; (b) Tang, X.; Sun, Y.; Zeng, X.; Hao, W.; Lin, L.; Liu, S., Novel process for the extraction of ethyl levulinate by toluene with less humins from the ethanolysis products of carbohydrates. *Energy Fuels* **2014**, *28* (7), 4251–4255.
37. Wettstein, S. G.; Alonso, D. M.; Chong, Y.; Dumesic, J. A., Production of levulinic acid and gamma-valerolactone (GVL) from cellulose using GVL as a solvent in biphasic systems. *Energy Environ. Sci.* **2012**, *5* (8), 8199–8203.

38. Manzer, L. E., Catalytic synthesis of alpha-methylene-gamma-valerolactone: a biomass-derived acrylic monomer. *Appl Catal a-Gen* **2004**, *272* (1–2), 249–256.
39. Yan, Z. P.; Lin, L.; Liu, S. J., Synthesis of gamma-valerolactone by hydrogenation of biomass-derived Levulinic Acid over Ru/C Catalyst. *Energ Fuel* **2009**, *23* (8), 3853–3858.
40. Hengne, A. M.; Rode, C. V., Cu-ZrO₂ nanocomposite catalyst for selective hydrogenation of levulinic acid and its ester to γ -valerolactone. *Green Chem.* **2012**, *14* (4), 1064–1072.
41. Yan, K.; Liao, J.; Wu, X.; Xie, X., A noble-metal free Cu-catalyst derived from hydrotalcite for highly efficient hydrogenation of biomass-derived furfural and levulinic acid. *RSC Adv.* **2013**, *3* (12), 3853–3856.
42. Di Mondo, D.; Ashok, D.; Waldie, F.; Schrier, N.; Morrison, M.; Schlaf, M., Stainless steel as a catalyst for the total deoxygenation of glycerol and levulinic acid in aqueous acidic medium. *ACS Catal.* **2011**, *1* (4), 355–364.
43. Mehdi, H.; Fabos, V.; Tuba, R.; Bodor, A.; Mika, L. T.; Horvath, I. T., Integration of homogeneous and heterogeneous catalytic processes for a multi-step conversion of biomass: From sucrose to levulinic acid, gamma-valerolactone, 1,4-pentanediol, 2-methyl-tetrahydrofuran, and alkanes. *Top Catal* **2008**, *48* (1–4), 49–54.
44. Heeres, H.; Handana, R.; Chunai, D.; Rasrendra, C. B.; Girisuta, B.; Heeres, H. J., Combined dehydration/(transfer)-hydrogenation of C₆-sugars (D-glucose and D-fructose) to gamma-valerolactone using ruthenium catalysts. *Green Chem* **2009**, *11* (8), 1247–1255.
45. Bourne, R. A.; Stevens, J. G.; Ke, J.; Poliakoff, M., Maximising opportunities in supercritical chemistry: the continuous conversion of levulinic acid to gamma-valerolactone in CO₂. *Chem Commun* **2007**, (44), 4632–4634.
46. Alonso, D. M.; Wettstein, S. G.; Bond, J. Q.; Root, T. W.; Dumesic, J. A., Production of biofuels from cellulose and corn stover using alkylphenol solvents. *Chemsuschem* **2011**, *4* (8), 1078–1081.
47. Raoufmoghaddam, S.; Rood, M. T. M.; Buijze, F. K. W.; Drent, E.; Bouwman, E., Catalytic conversion of γ -valerolactone to ϵ -caprolactam: Towards Nylon from renewable feedstock. *Chemsuschem* **2014**, *7* (7), 1984–1990.
48. Huber, G. W.; Iborra, S.; Corma, A., Synthesis of transportation fuels from biomass: chemistry, catalysts, and engineering. *Chem Rev* **2006**, *106* (9), 4044–4098.
49. (a) Bond, J. Q.; Alonso, D. M.; Wang, D.; West, R. M.; Dumesic, J. A., Integrated catalytic conversion of gamma-valerolactone to liquid alkenes for transportation fuels.

- Science* **2010**, 327 (5969), 1110–1114; (b) Bond, J. Q.; Upadhye, A. A.; Olcay, H.; Tompsett, G. A.; Jae, J.; Xing, R.; Alonso, D. M.; Wang, D.; Zhang, T. Y.; Kumar, R.; Foster, A.; Sen, S. M.; Maravelias, C. T.; Malina, R.; Barrett, S. R. H.; Lobo, R.; Wyman, C. E.; Dumesic, J. A.; Huber, G. W., Production of renewable jet fuel range alkanes and commodity chemicals from integrated catalytic processing of biomass. *Energ Environ Sci* **2014**, 7 (4), 1500–1523.
50. Serrano-Ruiz, J. C.; Wang, D.; Dumesic, J. A., Catalytic upgrading of levulinic acid to 5-nonanone. *Green Chem* **2010**, 12 (4), 574–577.
51. Serrano-Ruiz, J. C.; West, R. M.; Dumesic, J. A., Catalytic conversion of renewable biomass resources to fuels and chemicals. *Annu Rev Chem Biomol* **2010**, 1, 79–100.
52. Bond, J. Q.; Wang, D.; Alonso, D. M.; Dumesic, J. A., Interconversion between γ -valerolactone and pentenoic acid combined with decarboxylation to form butene over silica/alumina. *J. Catal.* **2011**, 281 (2), 290–299.
53. Bond, J. Q.; Martin Alonso, D.; West, R. M.; Dumesic, J. A., γ -Valerolactone ring-opening and decarboxylation over $\text{SiO}_2/\text{Al}_2\text{O}_3$ in the presence of water. *Langmuir* **2010**, 26 (21), 16291–16298.
54. Gaussian 09, Revision E.01, Frisch, M. J.; Trucks, G. W.; Schlegel, H. B.; Scuseria, G. E.; Robb, M. A.; Cheeseman, J. R.; Scalmani, G.; Barone, V.; Mennucci, B.; Petersson, G. A.; Nakatsuji, H.; Caricato, M.; Li, X.; Hratchian, H. P.; Izmaylov, A. F.; Bloino, J.; Zheng, G.; Sonnenberg, J. L.; Hada, M.; Ehara, M.; Toyota, K.; Fukuda, R.; Hasegawa, J.; Ishida, M.; Nakajima, T.; Honda, Y.; Kitao, O.; Nakai, H.; Vreven, T.; Montgomery, J. A., Jr.; Peralta, J. E.; Ogliaro, F.; Bearpark, M.; Heyd, J. J.; Brothers, E.; Kudin, K. N.; Staroverov, V. N.; Kobayashi, R.; Normand, J.; Raghavachari, K.; Rendell, A.; Burant, J. C.; Iyengar, S. S.; Tomasi, J.; Cossi, M.; Rega, N.; Millam, J. M.; Klene, M.; Knox, J. E.; Cross, J. B.; Bakken, V.; Adamo, C.; Jaramillo, J.; Gomperts, R.; Stratmann, R. E.; Yazyev, O.; Austin, A. J.; Cammi, R.; Pomelli, C.; Ochterski, J. W.; Martin, R. L.; Morokuma, K.; Zakrzewski, V. G.; Voth, G. A.; Salvador, P.; Dannenberg, J. J.; Dapprich, S.; Daniels, A. D.; Farkas, Ö.; Foresman, J. B.; Ortiz, J. V.; Cioslowski, J.; Fox, D. J. Gaussian, Inc., Wallingford CT, 2009.
55. Kellicutt, A. B.; Salary, R.; Abdelrahman, O. A.; Bond, J. Q., An examination of the intrinsic activity and stability of various solid acids during the catalytic decarboxylation of γ -valerolactone. *Catal. Sci. Technol.* **2014**, 4 (8), 2267–2279.
56. Vannice, M. A., *Kinetics of Catalytic Reactions*. Springer: New York, 2005
57. Storck, S.; Bretinger, H.; Maier, W. F., Characterization of micro- and mesoporous solids by physisorption methods and pore-size analysis. *Appl Catal a-Gen* **1998**, 174 (1–2), 137–146.

58. (a) Campbell, C. T.; Lytken, O., Experimental measurements of the energetics of surface reactions. *Surf Sci* **2009**, *603* (10–12), 1365–1372; (b) Stegelmann, C.; Andreasen, A.; Campbell, C. T., Degree of Rate Control: How much the energies of intermediates and transition states control rates (vol 131, pg 8077, 2009). *J Am Chem Soc* **2009**, *131* (37), 13563–13563.
59. Bond, J. Q.; Alonso, D. M.; West, R. M.; Dumesic, J. A., gamma-Valerolactone ring-opening and decarboxylation over SiO₂/Al₂O₃ in the presence of water. *Langmuir* **2010**, *26* (21), 16291–16298.
60. G, P. R., Hard and soft acids and bases. *J. Am. Chem. Soc* **1963**, *85* (22), 3533–3539.
61. Robert G. Parr, R. G. P., Absolute hardness: companion parameter to absolute electronegativity *J. Am. Chem. Soc.* **1983**, *105* (26), 7512–7516.
62. Waugh, K. C., Prediction of global reaction kinetics by solution of the Arrhenius parameterised component elementary reactions: microkinetic analysis. *Catal Today* **1999**, *53* (2), 161–176.
63. Dumesic, J. A.; Milligan, B. A.; Greppi, L. A.; Balse, V. R.; Sarnowski, K. T.; Beall, C. E.; Kataoka, T.; Rudd, D. F.; Trevino, A. A., A Kinetic Modeling approach to the design of catalysts - formulation of a catalyst design advisory program. *Ind Eng Chem Res* **1987**, *26* (7), 1399–1407.

VITA

NAME OF AUTHOR:

Christian Suhngwa Jungong

PLACE OF BIRTH:

Bamenda, Cameroon

UNDERGRADUATE & GRADUATE SCHOOLS ATTENDED:

University of Buea, Cameroon

University of North Dakota, UND, Grand Forks, ND

DEGREES AWARDED:

Bachelor of Science in Chemistry, 2006, University of Buea

Doctor of Philosophy in Organic Synthesis, 2012, UND

AWARDS AND HONORS:

Roland Severson Award for outstanding graduate research, 2010

Ernest D. Coon Award for outstanding graduate teaching, 2010

Doctoral student travel awards, 2010 & 2012